

THE ACS NEARBY GALAXY SURVEY TREASURY I. THE STAR FORMATION HISTORY OF THE M81 OUTER DISK

BENJAMIN F. WILLIAMS¹, JULIANNE J. DALCANTON¹, ANIL C. SETH², DANIEL WEISZ³, ANDREW DOLPHIN⁴, EVAN SKILLMAN³, JASON HARRIS⁵, JON HOLTZMAN⁶, LÉO GIRARDI⁷, ROELOF S. DE JONG⁸, KNUT OLSEN⁹, ANDREW COLE¹⁰, CARME GALLART¹¹, STEPHANIE M. GOGARTEN¹, SEBASTIAN L. HIDALGO³, MARIO MATEO¹², KEITH ROSEMA¹, PETER B. STETSON¹³, THOMAS QUINN¹

Draft version November 6, 2018

ABSTRACT

The ACS Nearby Galaxy Survey Treasury (ANGST) is a large *Hubble Space Telescope* (*HST*) Advanced Camera for Surveys (ACS) treasury program to obtain resolved stellar photometry for a volume-limited sample of galaxies out to 4 Mpc. As part of this program, we have obtained deep ACS imaging of a field in the outer disk of the large spiral galaxy M81. The field contains the outskirts of a spiral arm as well as an area containing no current star formation. Our imaging results in a color-magnitude diagram (CMD) reaching to $m_{F814W} = 28.8$ and $m_{F606W} = 29.5$, one magnitude fainter than the red clump. Through detailed modeling of the full CMD, we quantify the age and metallicity distribution of the stellar populations contained in the field. The mean metallicity in the field is $-1 < [M/H] < 0$ and only a small fraction of stars have ages $\lesssim 1$ Gyr. The results show that most of the stars in this outer disk field were formed by $z \sim 1$ and that the arm structure at this radius has a lifetime of $\gtrsim 100$ Myr. We discuss the measured evolution of the M81 disk in the context of surveys of high-redshift disk galaxies and deep stellar photometry of other nearby galaxies. All of these indicate that massive spiral disks are mostly formed by $z \sim 1$ and that they have experienced rapid metal enrichment.

Subject headings: galaxies: individual (M81) — galaxies: stellar populations — galaxies: spiral — galaxies: evolution

1. INTRODUCTION

Analytic and numerical models indicate that spiral disks should grow and evolve with time due to continued gas accretion, interactions, spiral density waves, and internal viscous evolution (Fall & Efstathiou 1980; Dalcanton et al. 1997; Mo et al. 1998; van den Bosch 2001; Bell 2002; Shen & Sellwood 2006; Debattista et al. 2006; Governato et al. 2007). Current observational con-

straints on the evolution of disks have come largely through identifying changes in the bulk properties of the galaxy population from in situ measurements at high redshifts (up to $z \sim 1 - 1.5$). However, these observational attempts to confirm disk evolution models give conflicting results (Simard et al. 1999; Ravindranath et al. 2004; Trujillo et al. 2004; Barden et al. 2005; Melbourne et al. 2007; Cameron & Driver 2007), likely due to selection effects that are difficult to quantify. Fortunately, the evolution of disks can be independently constrained with photometry of the resolved stellar populations in nearby galaxies. Such photometry provides a fossil record of the formation and evolution of the disk and complements the findings of redshift surveys.

Resolved stellar photometry provides the most detailed data with which to determine the star formation history (SFH) of a galaxy. By fitting stellar evolution models to an observed color-magnitude diagram (CMD), we can recover the stellar ages and metallicities that best reproduce the color and magnitude distribution of a galaxy's stars. To fully tap this capability, the ACS Nearby Galaxy Survey Treasury (ANGST) has undertaken a program to measure resolved stellar photometry for a volume-limited sample of galaxies (Dalcanton et al. 2008). Within this volume, large galaxies dominate the stellar mass. Of these, the largest and most well-studied at all wavelengths is M81, a massive SA(s)ab spiral disk at a distance of 3.9 Mpc (Tikhonov et al. 2005) with low foreground extinction ($A_V = 0.27$; Schlegel et al. 1998). Its luminosity ($M_K = -24$; Skrutskie et al. 2006) places it at $2.5L_*$ (assuming $M_{K*} = -23$; Kochanek et al. 2001), making it characteristic of the disk galaxies seen in redshift surveys out to $z \sim 1$ (e.g., Oyaizu et al. 2008).

¹ Department of Astronomy, Box 351580, University of Washington, Seattle, WA 98195; ben@astro.washington.edu; jd@astro.washington.edu; stephanie@astro.washington.edu; krosema@astro.washington.edu; trq@astro.washington.edu

² CFA Fellow, Harvard-Smithsonian Center for Astrophysics, 60 Garden Street, Cambridge, MA 02138; aseth@cfa.harvard.edu

³ Department of Astronomy, University of Minnesota, 116 Church St. SE, Minneapolis, MN 55455; dweisz@astro.umn.edu; skillman@astro.umn.edu; slhidalgo@astro.umn.edu

⁴ Raytheon, 1151 E. Hermans Road, Tucson, AZ 85706; dolphin@raytheon.com

⁵ Steward Observatory, University of Arizona, 933 North Cherry Avenue, Tucson, AZ 85721; jharris@as.arizona.edu

⁶ Department of Astronomy, New Mexico State University, Box 30001, 1320 Frenger St., Las Cruces, NM 88003; holtz@nmsu.edu

⁷ Osservatorio Astronomico di Padova - INAF, Vicolo dell'Osservatorio 5, I-35122 Padova, Italy; leo.girardi@oapd.inaf.it

⁸ Space Telescope Science Institute, Baltimore, MD 21218; dejong@stsci.edu

⁹ NOAO, CTIO, Casilla 603, La Serena, Chile; kolsen@ctio.noao.edu

¹⁰ School of Mathematics and Physics, University of Tasmania, Hobart, Tasmania, Australia; andrew.cole@utas.edu.au

¹¹ Instituto de Astrofísica de Canarias, Vía Lctea, s/n, 38200 La Laguna, Tenerife, SPAIN; carme@iac.es

¹² Department of Astronomy, University of Michigan, 830 Dennington Building, Ann Arbor, MI 48109-1090; mmateo@umich.edu

¹³ Dominion Astrophysical Observatory, Herzberg Institute of Astrophysics, National Research Council, 5071 West Saanich Road, Victoria, BC V9E 2E7, Canada; Peter.Stetson@nrc-cnrc.gc.ca

M81 provides a key laboratory for using resolved stellar photometry to look for relics of the evolution seen at high-redshift. Several surveys suggest that large disk galaxies like M81 have their disks in place by $z \sim 1$, after which luminosity evolution dominates (Lilly et al. 1998; Ravindranath et al. 2004; Papovich et al. 2005; Sargent et al. 2007; Melbourne et al. 2007). In this context, understanding the SFH of nearby large disk galaxies like M81 provides complementary insight into their evolution that is free of any biases contained in redshift survey samples.

Much work has been done to understand the evolution of M81 from its star clusters (Ma et al. 2005; Perelmuter et al. 1995), its X-ray source population (Swartz et al. 2003), and its young supergiant stars as seen in the near infrared (Davidge 2006). Its structure and evolution have been studied in detail from ultraviolet to radio (Pérez-González et al. 2006; Willner et al. 2004; Gordon et al. 2004; Li et al. 2004; Westpfahl 1998), but very little work has been done to integrate these results with the resolved stellar populations.

Most work on resolved stellar populations in M81 has relied on the *Hubble Space Telescope* (*HST*) to resolve the individual stars, as only stars brighter than the red giant branch (RGB) tip are resolved from the ground (e.g., Madore et al. 1993). Tikhonov et al. (2005) studied the resolved stellar populations of M81 with archival WFPC2 and ACS data, and there are several *HST* programs that are currently underway with greater depth and spatial coverage (de Jong et al. 2007; Sarajedini 2005; Zezas 2005; Huchra 2004). The results from these programs will allow detailed comparisons with those from integrated light studies.

Herein we describe the ANGST measurements of the SFH of the outer disk of M81 using F606W and F814W stellar photometry. The outer disk has low enough crowding that precision photometry can be obtained below the red clump with ACS, and provides leverage with which to potentially constrain size evolution of the galactic disk. §2 details our data acquisition and reduction techniques. §3 discusses our analysis of specific portions of the color-magnitude diagram (CMD), and §4 details our analysis of the full CMD to determine the SFH of the field. Finally, §5 summarizes the conclusions drawn from these results, placing our measurements in the context of disk galaxy surveys and resolved stellar populations of other large galaxies. We adopt a cosmology with $H = 73$ km s⁻¹ Mpc⁻¹, $\Omega_\Lambda = 0.76$, and $\Omega_M = 0.24$ for all look-back time calculations, and we assume a distance to M81 of 3.9 Mpc for conversions of angular measurements to physical distances.

2. DATA ACQUISITION AND REDUCTION

From 2006-Nov-16 to 2006-Nov-22, we observed a field in the outskirts of the M81 disk located at R.A. (2000) = 148.644625 (09:54:34.7), decl. (2000) = +69.2804 (+69:16:49.4) with a rotation angle PA_V3=89.81. Figure 1 shows an outline of the field location, which is 14' (16 kpc at M81) out along the major axis and corresponds to 5 scale lengths and 18 effective radii of the bulge ($h_r \sim 3$ kpc and bulge $R_e \sim 0.9$ kpc, Kendall et al. 2008). The equivalent location in M31, as shown on the inset in Figure 1, suggests that the disk population is likely to still dominate at this radius if M81 and M31

are similar. This suggestion is consistent with the ongoing analysis of de Jong et al. (2007), which finds that the halo population does not dominate until galactocentric distances $\gtrsim 20$ kpc.

We obtained 9 full-orbit exposures with the ACS (Ford et al. 1998) through the F606W (wide *V*) filter, and 11 full-orbit exposures through the F814W (*I* equivalent) filter. These data totaled 24132 s and 29853 s of exposure time in F606W and F814W, respectively. Routine image calibration, including bias corrections and flat-fielding, were performed by the *HST* pipeline, OPUS version 2006_5, CALACS version 4.6.1. We processed the images by running the `multidrizzle` task within PyRAF (Koekemoer et al. 2002). This procedure was used only to flag the cosmic rays in the individual images, after which, photometry was measured simultaneously for all of the objects in the uncombined images using the software package DOLPHOT (Dolphin 2000) including the ACS module. This package is optimized for measuring photometry of stars on ACS images using the well-characterized and stable point spread function (PSF), calculated with TinyTim.¹⁴ The software fits the PSF to all of the stars in each individual frame to find PSF magnitudes. It then determines and applies the aperture correction for each image using the most isolated stars, corrects for the charge transfer efficiency of the ACS detector, combines the results from the individual exposures, and converts the measured count rates to the VEGAMag system.

The DOLPHOT output was then filtered to only allow objects classified as stars with signal-to-noise >6 in both filters. The list was further culled using sharpness ($|F606W_{sharp} + F814W_{sharp}| < 0.27$) and crowding ($F606W_{crowd} + F814W_{crowd} < 0.1$). The sharpness cut was chosen based on the distribution of values in the original catalog. This distribution is shown in Figure 2 and flattens at a value of ~ 0.27 . The crowding parameter gives the difference between the magnitude of a star measured before and after subtracting the neighboring stars in the image. When this value is large, it suggests that the star's photometry was significantly affected by crowding, and we therefore exclude it from our catalog. Quality cuts based on the χ values were also considered, but they were rejected when a correlation was found between χ and the local background. Our final star catalog for the field contained 120912 stars detected in both F606W and F814W, and the resulting CMD is shown in Figure 3.

The same software package was used to perform artificial star tests using identical measurement techniques and quality cuts. We ran 2.5×10^6 artificial stars to characterize our photometry errors and completeness as a function of color, magnitude, and position. In each iteration, a single star was added to the images, and the photometry of the images was remeasured in the area where the star was added, including a radius of the PSF size plus the photometry aperture size to include the photometry of all stars whose photometry could be affected by the existence of the artificial star. Half of the artificial stars were sampled randomly in color and magnitude covering the full range present in our observed CMD plus an additional magnitude fainter to account for upscatter

¹⁴ <http://www.stsci.edu/software/tinytim/>

of faint stars into our recovered magnitude range. The other half were sampled following the color and magnitude distribution of our observed CMD after extrapolating the distribution to fainter magnitudes to account for upscatter. The artificial stars were distributed randomly over the field of view. The photometric errors measured from our tests are shown in Figure 5, and the completeness measured from our tests is shown in Figure 6. When fitting the color-magnitude distribution of the stars, we included only stars brighter than a 60% completeness limit as measured from the artificial star tests ($m_{F606W} = 29.1$ and $m_{F814W} = 28.4$). At this depth and this Galactic latitude ($b = 40.9^\circ$), the expected number of Galactic foreground stars is $\lesssim 20$ arcmin $^{-2}$, suggesting foreground contamination in our field of $\lesssim 200$ objects or $<0.2\%$ of the total number of stars.

3. RED CLUMP AND ASYMPTOTIC GIANT BRANCH BUMP ANALYSIS

3.1. Overview

Before attempting to understand the complexities of the CMD as a whole, we first focus on a few key stellar evolution features in our full-field CMD that help to give a broad sense of the range of ages and metallicities of the stars in the field (Figure 3). The vertical plume at $m_{F606W} - m_{F814W} = 0$ is due to the young population of stars that is still on the main sequence. The handful of stars populating the diagram brightward and slightly redward of this plume are massive core He-burning stars, which are young stars that have recently evolved off of the main sequence. We plot the spatial distribution of the main sequence stars in Figure 4; the young stars are clearly concentrated in the inner disk (seen in the bottom of the image) and in the extension of the spiral arm seen in Figure 1.

Several older populations are seen as well. The dense clump of stars at $m_{F814W} \sim 27.8$ is the red clump (Cannon 1970; Alves & Sarajedini 1999), which corresponds to the core-He burning phase of all intermediate-age and old populations which are neither too old, nor too metal-poor, to develop the horizontal branch. Brightward of this feature is another, less prominent peak, known as the asymptotic giant branch (AGB) bump (Gallart 1998), which corresponds to the so-called early-AGB phase of low-mass stars, during which He shell burning transits from a very extended to a thin shell. Extending vertically through both the red clump and AGB bump is a broad RGB with a well-defined tip, indicating the presence of a range of ages and metallicities in the field. Brightward of this tip is a relatively small number of thermally-pulsating AGB stars, i.e. stars in the stage of double shell burning which undergo recurrent He shell flashes. The most luminous among these thermally-pulsating AGB stars have intense winds that eventually shed their outer layers to become planetary nebulae.

3.2. Red Clump and AGB Bump Fitting Method

To investigate the general characteristics of the stellar populations in our field, we first performed precision measurements of the very well-defined red clump and AGB bump, seen at $m_{F814W} \sim 27.8$ and $m_{F814W} \sim 26.7$

in the diagrams in Figure 3 respectively. These are areas of the CMD containing a high density of stars, allowing their precise locations to be measured and directly compared to stellar evolution models. The colors and luminosities of these features have been used to constrain the properties of stellar populations (Rejkuba et al. 2005; Tanaka et al. 2008). We include such a measurement here to take advantage of the depth and quality of our photometry and to allow for intercomparisons with other such analyses. However, as we discuss below, uncertainties with the models of these discrete features substantially limit the interpretation of these measurements, making simultaneous fitting of the full CMD preferable; we present such fits in § 4.

We measured the magnitudes of the red clump and AGB bump by creating a magnitude histogram from our photometry and fitting it with a combination of a line and 2 Gaussians, following the methods of Rejkuba et al. (2005). We then fit Gaussians to histograms of slices through color space taken at the measured peak magnitudes (Figure 7). The red clump in this outer region of the M81 disk has $m_{F814W} = 27.792 \pm 0.002$ (FWHM=0.450) and $m_{F606W} - m_{F814W} = 0.855 \pm 0.001$ (FWHM=0.363). The AGB bump has $m_{F814W} = 26.72 \pm 0.01$ (FWHM=0.27) and $m_{F606W} - m_{F814W} = 0.974 \pm 0.002$ (FWHM=0.346). These are the raw measurements for these features; no extinction correction has been applied.

We then measured the locations of model red clumps and AGB bumps by populating the isochrones of Girardi et al. (2002) including updates of AGB models in Marigo et al. (2008).¹⁵ We used the StarFISH (Harris & Zaritsky 2001) task `testpop`, to produce a grid of CMDs for discrete ages and metallicities, assigning extinctions, distances, errors, and completeness measured from our data (see § 4). We then ran our red clump and AGB bump fitting technique on this grid of model CMDs to measure the location of these features as a function of age and metallicity.

We determined the model red clump and AGB bump with F606W and F814W magnitudes closest to those observed in our field, assuming an adopted distance of $(m - M)_0 = 27.93$ and extinction of $A_V = 0.27$. These distance and extinction values resulted in a grid of model red clump and AGB bump values that did not intersect with our measured values. We therefore show a model grid with a farther assumed distance ($(m - M)_0 = 28.0$) and higher extinction ($A_V = 0.3$) in Figure 8, to produce a grid that does intersect with our observed values. From this analysis, the models suggest that the red clump is dominated by stars with an age of ~ 2 -3 Gyr and $[M/H] \sim -0.4$ and that the AGB bump is dominated by older, more metal-poor stars with an age of ~ 10 Gyr and $[M/H] \sim -0.7$.

Because the precise colors and magnitudes of the red clump and AGB bump do not provide reliable conclusions (see S 3.3), we also investigated the relative numbers of stars contained within the red clump and AGB bump features. This measurement should be insensitive to distance and extinction. We calculated the integral of the functional fit to the magnitude histogram including and excluding the Gaussian terms corresponding to each

¹⁵ <http://stev.oapd.inaf.it/cmd>

feature. The difference between these integrals provided the number of stars within each feature. The ratio of the number of stars in the AGB bump to that contained in the red clump ($N_{AGBb} : N_{RC}$) was 0.044 ± 0.008 . Errors are the standard deviation of the same measurement made on 100 random samples of our data and are dominated by the small number of stars in the AGB bump. Comparing this range of ratios to the ratios obtained by running the same calculations on the functional fits to models suggests that the dominant stellar population of our sample is metal-rich and older than 3 Gyr (see Figure 9). The ratio is therefore consistent with the color and magnitude of the model AGB, but less so with those of the red clump, in that the model red clump is fainter than it should be for a population old enough to have this fraction of AGB bump stars.

3.3. Interpretation of Red Clump and AGB Bump Fitting Results

Although analyses similar to those above are becoming common, the red clump and AGB-bump colors, magnitudes, and relative numbers cannot provide conclusive results about the age and metallicity distribution of the population. The reasons for the inconclusive results include the sensitivity of the results to known deficiencies of stellar evolution models as well as to the assumed distance and reddening of the stars in the CMD.

We found our fits to the color and magnitude of the red clump and AGB bump difficult to interpret because they are particularly sensitive to weaknesses of the stellar evolution models. The majority of the red clump models are faint compared to our observed red clump. While the trends of the colors and luminosities of the red clump and AGB bump with age and metallicity (older and more metal-rich are fainter and redder) are robust against model updates and different model prescriptions, the absolute colors and luminosities are less stable. For example, red clump model luminosities depend primarily on opacities and neutrino losses during the previous RGB phase, which are still subject to significant variations in the literature. Girardi et al. (2002) models of the red clump are known to be some of the faintest because of their treatment of these processes (Castellani et al. 2000). This effect can be seen in Figure 8, where nearly all of the model red clumps are fainter than our observed red clump even though most of the model AGB bumps are brighter than our observed AGB bump.

The $N_{AGBb} : N_{RC}$ ratio is also difficult to interpret. The ratio predicted by the models is sensitive to the assumed helium content and the treatment of convective cores, including complex processes such as overshooting and semiconvection, rendering any conclusions based on this ratio alone unreliable.

Furthermore, fits to the color and magnitude of the red clump and AGB bump depend on the extinction and distance values applied to the models, as changes of only ~ 0.1 mag in color or luminosity of the features correspond to differences of ~ 0.3 dex in metallicity and $\log(\text{age})$. The effects of distance and reddening uncertainty are shown with the arrows in Figure 8. While the adopted distance affects mainly the measured age, the adopted reddening largely affects the measured metallicity. More specifically, if we assume only foreground extinction value ($A_V = 0.27$), our best-

fitting ages remain the same, but the metallicities become $[M/H] \sim -0.4$ and $[M/H] \sim -0.1$ for the AGB bump and red clump, respectively. If we assume a distance modulus of $(m - M)_0 = 27.9$, the best-fitting ages and metallicities are $[M/H] \sim -0.7$, $[M/H] \sim -0.5$ and ~ 13 Gyr, ~ 5 Gyr for the AGB bump and red clump respectively.

In summary, while studying the red clump and AGB bump properties in detail is helpful for getting some sense of the overall age and metallicity of the population, or perhaps for constraining relative ages and metallicities among different galaxies, the results' sensitivity to uncertainties in stellar models, distance, and extinction, make this analysis less than optimal for obtaining reliable information about the stellar populations. Furthermore, no single age and metallicity will precisely fit the observed values because these features contain populations of a range of ages and metallicities. These difficulties with single component fitting make it necessary to perform more sophisticated statistical fits to the entire CMD to decipher the range of ages and metallicities present in our field. Full CMD fitting helps to reduce the effects of model deficiencies, providing an overall picture of the age and metallicity of the population even if some details of the models are wrong.

4. FULL CMD FITTING

4.1. Fitting Technique and Models Used

We measured the complete SFH, including the star formation rate and metallicity as functions of age, using the MATCH package (Dolphin 2002). This software fits the entire observed CMD by populating the stellar evolution models of Girardi et al. (2002, with updated AGB models from Marigo et al. 2008) with a given initial mass function (IMF), finding the distance modulus, extinction, and linear combination of ages and metallicities that best fit the observed color and magnitude distribution (see details in Dolphin 2002).

As was the case for the simplified AGB bump and red clump analysis, the results of full CMD fitting rely on the stellar evolution models used to fit the CMD. There are known discrepancies between different sets of stellar evolution models in the RGB, red clump, and AGB bump phases of evolution (see Figure 10 of Gallart et al. 2005). The reasons for the discrepancies are many, from the adopted input physics to the uncertainty in mass loss during the RGB and AGB phases of evolution. These differences affect the location and morphology of these regions of the observed CMD.

On the other hand, the shape of the red clump region does contain information about the SFH. The fitting algorithms are sensitive to this information if they are set to fit the distance and reddening values independently in order to compensate for offsets between model red clump positions. For instance, the RGB colors are sensitive to both age and metallicity, whereas the RGB-red clump color difference is more sensitive to the age (Hatzidimitriou 1991). While many age-metallicity models could fit the overall RGB color distribution, when the red clump is present its color difference forces the SFH-recovery towards the best-fitting age distribution, provided that it is allowed to fit also the red clump magnitude (e.g. by adjusting the distance). The final result is that this area of the CMD provides a reliable SFH,

even if the models for the red clump contain offsets. To test this point, we ran a different fitting code and stellar evolution library to fit our full-field data. We applied the IAC-STAR/IAC-POP/MINNIAC CMD fitting codes (Aparicio & Hidalgo 2004, 2008, Hidalgo, S. L. et al. 2008, AJ, in preparation) to our data using the BaSTI stellar evolution models (Pietrinferni et al. 2004). The broad trends on the resulting SFH were totally consistent.

This point is strengthened by the tests of Barker et al. (2007), who compared results for SFHs as determined with different sets of stellar evolution models and found differences in the details but agreement for general population characteristics. Furthermore, the results of Tolstoy et al. (1998) and Cole et al. (2007) show that, while SFHs based on the main-sequence turnoff provide more reliable age information at older ages than those from shallower photometry, the general trends determined in shallower photometry are robust. To avoid drawing conclusions based on the finest details in age and metallicity applied to fit the CMD (see § 4.3), we bin our results to an age and metallicity resolution where both the CMD fitting method and stellar evolution models are well-tested and the limitations are known.

4.2. Field Division

Our field contained a portion of a spiral arm running through the north and east portion of the image. The bifurcated arm, which may have been created by an interaction, can be seen in the locations of the main-sequence stars, which are mainly limited to the northeast portion and the southeast corner (Figure 4). This distribution shows that the northeast spiral arm is split, with a spur to the north, consistent with H I maps of Yun et al. (1994) and Adler & Westpfahl (1996). The recent star formation in this structure is likely to be at least partially due to a tidal stream from one of several recent interactions with other galaxies in the M81 group (Yun et al. 1994; Yun 1999). The southeast region of the image is more crowded as well, where it skims the inner disk.

For measuring the SFH, we divided the field into regions inside the arm, outside the arm, and the more crowded inner disk, as shown in Figure 4. Since the crowding and extinction are different in each of these subregions, we determined the error and completeness characteristics separately for each subregion. The final CMDs for the arm and interarm subregions are shown along with the full CMD in Figure 3.

4.3. Fitting Parameters

To model a full CMD, several fitting parameters must be chosen. These choices include the binary fraction, IMF slope, the area of the CMD to include in the fit, the approximate distance and mean extinction to the stars in the field, and the binning of the stellar evolution models in time and metallicity. Below we discuss how we chose these parameters and how the choices impact our results.

When populating the model isochrones, we assumed a binary fraction of 0.35 and a Salpeter (1955) IMF. As has been shown by other studies using this technique (e.g., Williams et al. 2007; Barker et al. 2007), for photometry that does not include the main sequence of old stars, the IMF assumed does not affect the relative star formation

rates in the SFH, but does affect the normalization of the SFH. This normalization effect occurs because the red clump, RGB, and AGB probe a narrow range of initial mass. Therefore changing the slope has little effect on the relative star formation rates, but a large effect on the extrapolation of the mass contained in the underlying unresolved low-mass main-sequence stars. Since we are not attempting to determine the precise star formation rate but rather are interested in the relative SFH within the field, a Salpeter IMF is sufficient for our purposes.

When fitting the color-magnitude distribution of the stars, we included all stars brighter than our 60% completeness limit for the full field to avoid large completeness corrections in our model fitting. This completeness cut corresponds to $m_{F606W} = 29.1$ and $m_{F814W} = 28.4$, and only stars brighter than these magnitudes were included in our model fits. We allowed the distance modulus to range from 27.75 to 28.2 and the extinction to range from $A_V = 0.1$ to $A_V = 0.7$, which allows MATCH to determine the systematic errors that result from small changes to these parameters and to optimize the overall CMD fit even in the presence of localized deficiencies in the model isochrones. While differential extinction can, in principle, be a problem for fitting a CMD with a single extinction value, our M81 field lies in a region with very little visible dust structure in *Spitzer* maps (Kendall et al. 2008). Furthermore, modest amounts of differential extinction have been shown to have little impact on the results of full CMD fitting (Williams 2002).

The best-fitting distances (see Table 1) were all consistent with $(m - M)_0 = 27.9$ within the errors, which agree with the Cepheid distance from the *HST* key project ($(m - M)_0 = 27.8 \pm 0.2$; Freedman et al. 1994) and the distance determined by measuring the tip of the RGB in archival WFPC2 photometry ($(m - M)_0 = 27.93 \pm 0.04$; Tikhonov et al. 2005).

The best-fitting extinction for the interarm region was consistent with the value of $A_V = 0.27$ obtained from Schlegel et al. (1998) for the Milky Way foreground extinction (see Table 1). We note that the arm subregion had a measured extinction value that was significantly higher than the Milky Way foreground, reflecting the higher dust content expected in the arm region.

We used a fine logarithmic time and metallicity resolution (0.1 dex) when fitting the CMD to allow the best possible fit to the data. The fit to the full data set is shown in Figures 10 and 11. The full CMD fitting confirms that the models are not able to perfectly reproduce the red clump and AGB bump, as expected from our discussion of uncertainties in § 3. These are the only two features of the CMD that show significant differences between the data and the best-fitting model (bottom-right panel of Figure 10), confirming that the models of these features still need improvement. After performing the full CMD fit, we binned the age and metallicity results to coarser time resolution to reduce our SFH errors. Therefore while our fit did not force the star formation rate or metallicity to be constant within a given temporal bin, our final SFHs only show the mean rate and metallicity within each temporal bin to avoid drawing conclusions based on details of the fit that may not be robust against changes in models and fitting methods.

4.4. Error Determination

In addition to measuring the most likely SFH for our field, we ran Monte Carlo tests to determine the random uncertainties of the fits. We generated CMDs by randomly drawing stars from our observed CMD, allowing each star to be drawn any number of times. We then measured SFHs for the resulting CMDs and calculated differences from the best-fit to the actual data. We generated 100 samples with the same number of stars as our observed CMD, adopting each of the SFHs measured from our data to determine the random errors for each subfield. These errors were then added in quadrature to the systematic errors, determined by fitting the CMDs with a range of possible distance and reddening values, to provide the our final errors on the rate, metallicity, and cumulative fraction of stars formed as a function of time.

We note that our choice of time bin widths was very coarse for ages >2 Gyr to reflect our sensitivity to age from the RGB and AGB. From $\sim 2\text{--}8$ Gyr ($9.3 < \log(\text{age}) < 9.9$), the age distribution comes mostly from the relatively small number of stars on the AGB, which is a very short-lived and difficult to model stage of evolution. From $8\text{--}14$ Gyr ($9.9 < \log(\text{age}) < 10.15$) age has very little effect on the morphology of the AGB and RGB features. In addition, our metallicity measurements at young ages (<100 Myr) have large errors. Our only metallicity information for these ages comes from the relatively small number of stars on the short-lived He-burning sequences. Despite these unavoidable sources of uncertainty in age and metallicity, overall we are able to obtain very reliable estimates of the relative contributions of stars of old (>8 Gyr), intermediate ($2\text{--}8$ Gyr), and young (<2 Gyr) ages. Furthermore, we obtain reliable metallicities covering all but the youngest ages. Finally, the cumulative age distribution is stable against uncertainties at intermediate ages because systematic errors in the star formation rates in adjacent time bins are typically anti-correlated.

4.5. The SFH of the Full Field

The SFH of the entire field and the three independent subfields are shown in Figures 12–17. For the history of star formation in the full field (Figure 12 and Table 2), we find that more than 50% of the stars currently at 5 scale lengths from the galactic center formed by $z \sim 1$, and $\sim 70\%$ formed by $z \sim 0.5$. The bulk of the stars have $-1 \lesssim [M/H] \lesssim 0$, with no significant metallicity difference between the arm and interarm regions and with no evidence for a significant metal-poor component. Such a metallicity is consistent with the mean metallicities found by Tikhonov et al. (2005, $\langle [M/H] \rangle \sim -0.65$) from stellar photometry in 5 WFPC2 fields spanning a range of galactocentric distances out to ~ 5 scale lengths. It therefore appears that M81 was chemically enriched very early in its history. Moreover, the metallicity has not changed by more than ~ 1.0 dex (and possibly as little as 0.5 dex) since its very early history.

Although our metallicity results for recent times have large errors, their values ($-0.5 < [M/H] < 0.0$ at ages from 10 Myr to 100 Myr; Figure 12) are consistent with the gas-phase metallicity at this radius ($[O/H] \sim -0.3$) inferred from the abundance gradients of Zaritsky et al. (1994), suggesting that the gas responsible for this structure is from M81 and not recently accreted gas from

a more metal-poor interacting satellite. However, this metallicity does not rule out the possibility that the gas came from a metal-rich satellite, such as NGC 3077 ($[M/H] \sim 0$, Martin 1997).

4.6. The SFHs of the Subregions

Figure 16 shows the SFHs of the three subregions overplotted with the SFH of the total field. It is clear that the sum of the results of the three subregions measured independently is consistent with the result of the entire field measured at once. The consistency between the 3 independently measured SFHs and the total SFH for the field confirms that our measurement technique provides reliable and consistent results in a field containing regions with moderately different crowding and extinction properties. Furthermore, the more crowded portion of the field, closest to the galaxy center, has a SFH more similar to that of the interarm region than to that of the arm region, showing that this area is not part of an arm and is of higher density only because it is closer to the galaxy center.

While these three regions should have obvious differences in their recent SFHs (based on the distribution of main sequence stars; cf. Figure 4), the older stellar populations should be well mixed on timescales longer than the dynamical time ($\gtrsim 0.5$ Gyr). Indeed, we measure similar SFHs at times $\gtrsim 0.5$ Gyr. At younger ages, the interarm region shows a clear deficit of stars younger than a few hundred Myr. Fractionally, this difference corresponds to $\sim 2\%$ of the total star formation (see Figure 17 and Table 2). The arm region of our field contains essentially all of the stars with ages $\lesssim 100$ Myr. This shows that the stars have not scattered out of the arm structure on this timescale. In addition, there is a significantly higher fraction of stars with ages $\lesssim 0.5$ Gyr in the arm region than in the other regions. It therefore appears that the arm structure in this region has a lifetime of $\gtrsim 100$ Myr and that full dispersion occurs on a timescale of ~ 0.5 Gyr. The characteristic width of the arm region, divided by the typical lifetime gives an approximate speed for the diffusion of stars. Assuming an arm width of ~ 1 kpc (Westpfahl 1998) divided by a lifetime of ~ 100 Myr yields a diffusion speed of ~ 10 km s $^{-1}$, which is similar to the velocity dispersion of B stars in the Milky Way disk (Dehnen & Binney 1998). Therefore the timescales we are measuring for this arm feature are consistent with the stellar kinematics of our own Galactic disk. Since our data contain main-sequence and He-burning sequence information for the populations of these ages, spatially resolved SFHs, with a time resolution of ~ 25 Myr over the last ~ 300 Myr are currently in progress and will be presented in future papers (Gogarten et al. 2008; B. Williams et al., in preparation).

5. CONCLUSIONS

We have performed deep resolved stellar photometry of an ACS field in the outer disk of M81. The metallicities of the stars in the field appear to have increased by at most ~ 0.5 dex over the past 10 Gyr from $-1.0 \lesssim [M/H] \lesssim -0.5$ to $-0.5 \lesssim [M/H] \lesssim 0$, suggesting early enrichment and a mechanism at work diluting the enrichment products of roughly continuous star formation.

Similar behavior has been seen in the thick disk of the Milky Way and several other nearby large galaxies.

Figure 18 shows the metallicities of the dominant stellar population for several nearby galaxies and the Milky Way thick disk as a function of galaxy luminosity, field location, and dominant stellar age. The Milky Way thick disk has characteristic ages of 9–12 Gyr and metallicities of $[M/H] \gtrsim -0.7$ (Gilmore et al. 1995; Prochaska et al. 2000; Allende Prieto et al. 2006). Thick disks in somewhat smaller galaxies also appear to have metallicities >-1.0 (Seth et al. 2005). In addition, deep *HST* photometry of the M31 disk has revealed populations dominated by stars in this age and metallicity range (Williams 2002; Olsen et al. 2006; Brown et al. 2006), as has deep photometry of the outer disk of M33 (Barker et al. 2007). All of these results suggest that the histories of these large disk galaxies may have been similar.

Furthermore, even in the outskirts of large ellipticals, such as NGC 5128 ($[M/H] \sim -0.6$ and age ~ 8 Gyr, Rejkuba et al. 2005) and NGC 3377 (Harris et al. 2007, $[M/H] \sim -0.6$ and age >3 Gyr.), the age and metallicity of the dominating population is similar to that seen in the outer regions of M81 and other large disks. Taken together, these data point to a large galaxy formation scenario with rapid early enrichment to $[M/H] \gtrsim -1.0$, before lookback times of ~ 7 Gyr ($z > 0.9$).

There is also significant evidence that most of the stars in this field were formed by $z \sim 1$. Such a result is in general agreement with the findings of several recent galaxy surveys, which find that the disk galaxy population appears to have undergone little

growth since $z \sim 1$ (e.g., Melbourne et al. 2007; Sargent et al. 2007; Papovich et al. 2005; Barden et al. 2005; Ravindranath et al. 2004; Lilly et al. 1998). While M81 is only one large disk galaxy and our field is only a small portion of it, the similarity to Milky Way, M31, and even lower mass M33's stellar populations supports the same scenario. Measurements of the stellar populations of local disks therefore strengthen the results of some galaxy surveys by attacking the problem with a completely independent technique and finding a similar result.

Finally, the spatial distribution of main-sequence stars in the field show that the field partially covers the outskirts of a spiral arm as well as an interarm region. Detailed analysis of the resulting CMDs for the contrasting regions shows that the difference between the populations is due to the fraction of stars with ages younger than ~ 0.5 Gyr ago and results from only a small percentage ($\sim 2\%$) of the stars, similar to the arm and interarm populations seen in M31 disk populations (Williams 2002). In addition, stars younger than ~ 100 Myr appear to be confined to the arm region, suggesting the structure survives for at least 100 Myr.

Support for this work was provided by NASA through grant GO-10915 from the Space Telescope Science Institute, which is operated by the Association of Universities for Research in Astronomy, Incorporated, under NASA contract NAS5-26555.

REFERENCES

- Adler, D. S., & Westpfahl, D. J. 1996, *AJ*, 111, 735
 Allende Prieto, C., Beers, T. C., Wilhelm, R., Newberg, H. J., Rockosi, C. M., Yanny, B., & Lee, Y. S. 2006, *ApJ*, 636, 804
 Alves, D. R., & Sarajedini, A. 1999, *ApJ*, 511, 225
 Aparicio, A., & Gallart, C. 2004, *AJ*, 128, 1465
 Aparicio, A., & Hidalgo, S. L. 2008, *ApJ*, submitted
 Barden, M., et al. 2005, *ApJ*, 635, 959
 Barker, M. K., Sarajedini, A., Geisler, D., Harding, P., & Schommer, R. 2007, *AJ*, 133, 1138
 Bell, E. F. 2002, *ApJ*, 581, 1013
 Brown, T. M., Smith, E., Ferguson, H. C., Rich, R. M., Guhathakurta, P., Renzini, A., Sweigart, A. V., & Kimble, R. A. 2006, *ApJ*, 652, 323
 Cameron, E., & Driver, S. P. 2007, *MNRAS*, 377, 523
 Cannon, R. D. 1970, *MNRAS*, 150, 111
 Castellani, V., Degl'Innocenti, S., Girardi, L., Marconi, M., Prada Moroni, P. G., & Weiss, A. 2000, *A&A*, 354, 150
 Cole, A. A., et al. 2007, *ApJ*, 659, L17
 Dalcanton, J. J., et al. 2008, *ApJ*, submitted
 Dalcanton, J. J., Spergel, D. N., & Summers, F. J. 1997, *ApJ*, 482, 659
 Davidge, T. J. 2006, astro-ph/0610646
 de Jong, R. S., Radburn-Smith, D. J., & Sick, J. N. 2007, *ArXiv e-prints*, 0710.5511
 Debattista, V. P., Mayer, L., Carollo, C. M., Moore, B., Wadsley, J., & Quinn, T. 2006, *ApJ*, 645, 209
 Dehnen, W., & Binney, J. J. 1998, *MNRAS*, 298, 387
 Dolphin, A. E. 2000, *PASP*, 112, 1383
 Dolphin, A. E. 2002, *MNRAS*, 332, 91
 Fall, S. M., & Efstathiou, G. 1980, *MNRAS*, 193, 189
 Ferguson, A. M. N., Irwin, M. J., Ibata, R. A., Lewis, G. F., & Tanvir, N. R. 2002, *AJ*, 124, 1452
 Ford, H. C., et al. 1998, in Presented at the Society of Photo-Optical Instrumentation Engineers (SPIE) Conference, Vol. 3356, Proc. SPIE Vol. 3356, p. 234-248, Space Telescopes and Instruments V, Pierre Y. Bely; James B. Breckinridge; Eds., ed. P. Y. Bely & J. B. Breckinridge, 234
 Freedman, W. L., et al. 1994, *ApJ*, 427, 628
 Gallart, C. 1998, *ApJ*, 495, L43
 Gallart, C., Zoccali, M., & Aparicio, A. 2005, *ARA&A*, 43, 387
 Gilmore, G., Wyse, R. F. G., & Jones, J. B. 1995, *AJ*, 109, 1095
 Girardi, L., Bertelli, G., Bressan, A., Chiosi, C., Groenewegen, M. A. T., Marigo, P., Salasnich, B., & Weiss, A. 2002, *A&A*, 391, 195
 Gogarten, S. M., et al. 2008, *ApJ*, submitted
 Gordon, K. D., et al. 2004, *ApJS*, 154, 215
 Governato, F., Willman, B., Mayer, L., Brooks, A., Stinson, G., Valenzuela, O., Wadsley, J., & Quinn, T. 2007, *MNRAS*, 374, 1479
 Harris, J., & Zaritsky, D. 2001, *ApJS*, 136, 25
 Harris, W. E., Harris, G. L. H., Layden, A. C., & Stetson, P. B. 2007, *AJ*, 134, 43
 Hatzidimitriou, D. 1991, *MNRAS*, 251, 545
 Huchra, J. 2004, in HST Proposal, 6568
 Kendall, S., Kennicutt, R. C., Clarke, C., & Thornley, M. D. 2008, *ArXiv e-prints*, 0804.2380
 Kochanek, C. S., et al. 2001, *ApJ*, 560, 566
 Koekemoer, A. M., Fruchter, A. S., Hook, R. N., & Hack, W. 2002, in The 2002 HST Calibration Workshop : Hubble after the Installation of the ACS and the NICMOS Cooling System, Proceedings of a Workshop held at the Space Telescope Science Institute, Baltimore, Maryland, October 17 and 18, 2002. Edited by Santiago Arribas, Anton Koekemoer, and Brad Whitmore. Baltimore, MD: Space Telescope Science Institute, 2002., p.337, ed. S. Arribas, A. Koekemoer, & B. Whitmore, 337
 Li, J.-L., Zhou, X., Ma, J., & Chen, J.-S. 2004, *Chinese Journal of Astronomy and Astrophysics*, 4, 143
 Lilly, S., et al. 1998, *ApJ*, 500, 75
 Ma, J., Zhou, X., Chen, J., Wu, Z., Yang, Y., Jiang, Z., & Wu, J. 2005, *PASP*, 117, 256
 Madore, B. F., Freedman, W. L., & Lee, M. G. 1993, *AJ*, 106, 2243
 Marigo, P., Girardi, L., Bressan, A., Groenewegen, M. A. T., Silva, L., & Granato, G. L. 2008, *A&A*, 482, 883
 Martin, C. L. 1997, *ApJ*, 491, 561
 Melbourne, J., Phillips, A. C., Harker, J., Novak, G., Koo, D. C., & Faber, S. M. 2007, *ApJ*, 660, 81

- Mo, H. J., Mao, S., & White, S. D. M. 1998, *MNRAS*, 295, 319
- Mouhcine, M. 2006, *ApJ*, 652, 277
- Olsen, K. A. G., Blum, R. D., Stephens, A. W., Davidge, T. J., Massey, P., Strom, S. E., & Rigaut, F. 2006, *AJ*, 132, 271
- Oyaizu, H., Lima, M., Cunha, C. E., Lin, H., Frieman, J., & Sheldon, E. S. 2008, *ApJ*, 674, 768
- Papovich, C., Dickinson, M., Giavalisco, M., Conselice, C. J., & Ferguson, H. C. 2005, *ApJ*, 631, 101
- Perelmuter, J.-M., Brodie, J. P., & Huchra, J. P. 1995, *AJ*, 110, 620
- Pérez-González, P. G., et al. 2006, *ApJ*, 648, 987
- Pietrinferni, A., Cassisi, S., Salaris, M., & Castelli, F. 2004, *ApJ*, 612, 168
- Prochaska, J. X., Naumov, S. O., Carney, B. W., McWilliam, A., & Wolfe, A. M. 2000, *AJ*, 120, 2513
- Ravindranath, S., et al. 2004, *ApJ*, 604, L9
- Rejkuba, M., Greggio, L., Harris, W. E., Harris, G. L. H., & Peng, E. W. 2005, *ApJ*, 631, 262
- Sakai, S., et al. 2000, *ApJ*, 529, 698
- Salpeter, E. E. 1955, *ApJ*, 121, 161
- Sarajedini, A. 2005, in *HST Proposal*, 6924
- Sargent, M. T., et al. 2007, *ApJS*, 172, 434
- Schlegel, D. J., Finkbeiner, D. P., & Davis, M. 1998, *ApJ*, 500, 525
- Seth, A. C., Dalcanton, J. J., & de Jong, R. S. 2005, *AJ*, 130, 1574
- Shen, J., & Sellwood, J. A. 2006, *MNRAS*, 370, 2
- Simard, L., et al. 1999, *ApJ*, 519, 563
- Skrutskie, M. F., et al. 2006, *AJ*, 131, 1163
- Swartz, D. A., Ghosh, K. K., McCollough, M. L., Pannuti, T. G., Tennant, A. F., & Wu, K. 2003, *ApJS*, 144, 213
- Tanaka, M., Chiba, M., Komiyama, Y., Iye, M., & Guhathakurta, P. 2008, in *Mapping the Galaxy and Nearby Galaxies*, ed. K. Wada & F. Combes, 381
- Tikhonov, N. A., Galazutdinova, O. A., & Drozdovsky, I. O. 2005, *A&A*, 431, 127
- Tolstoy, E., et al. 1998, *AJ*, 116, 1244
- Tremonti, C. A., et al. 2004, *ApJ*, 613, 898
- Trujillo, I., et al. 2004, *ApJ*, 604, 521
- van den Bosch, F. C. 2001, *MNRAS*, 327, 1334
- Verheijen, M. A. W. 2001, *ApJ*, 563, 694
- Westpfahl, D. J. 1998, *ApJS*, 115, 203
- Williams, B. F. 2002, *MNRAS*, 331, 293
- Williams, B. F., et al. 2007, *ApJ*, 656, 756
- Willner, S. P., et al. 2004, *ApJS*, 154, 222
- Yun, M. S. 1999, in *IAU Symposium*, Vol. 186, *Galaxy Interactions at Low and High Redshift*, ed. J. E. Barnes & D. B. Sanders, 81
- Yun, M. S., Ho, P. T. P., & Lo, K. Y. 1994, *Nature*, 372, 530
- Zaritsky, D., Kennicutt, R. C., Jr., & Huchra, J. P. 1994, *ApJ*, 420, 87
- Zezas, A. 2005, in *HST Proposal*, 6904

TABLE 1
DISTANCES AND EXTINCTION VALUES FROM MATCH

Subfield	$(m - M)_0$	A_V
Full	27.89 ± 0.05	0.38 ± 0.06
Arm	27.88 ± 0.08	0.45 ± 0.06
Interarm	27.92 ± 0.06	0.33 ± 0.06
Crowd	27.88 ± 0.06	0.32 ± 0.06

TABLE 2
CUMULATIVE FRACTION OF STARS FORMED AT EACH
AGE

Redshift	Age (Gyr)	Fraction of Stars Formed
0.001	0.01	$1.000^{+0.000}_{-0.000}$
0.002	0.03	$0.999^{+0.000}_{-0.000}$
0.004	0.05	$0.999^{+0.000}_{-0.000}$
0.006	0.08	$0.999^{+0.000}_{-0.000}$
0.010	0.13	$0.999^{+0.000}_{-0.001}$
0.015	0.20	$0.997^{+0.001}_{-0.001}$
0.024	0.32	$0.994^{+0.001}_{-0.002}$
0.049	0.63	$0.979^{+0.006}_{-0.006}$
0.216	2.51	$0.848^{+0.069}_{-0.070}$
1.080	7.94	$0.622^{+0.055}_{-0.066}$
...	14.1	$0.000^{+0.000}_{-0.000}$

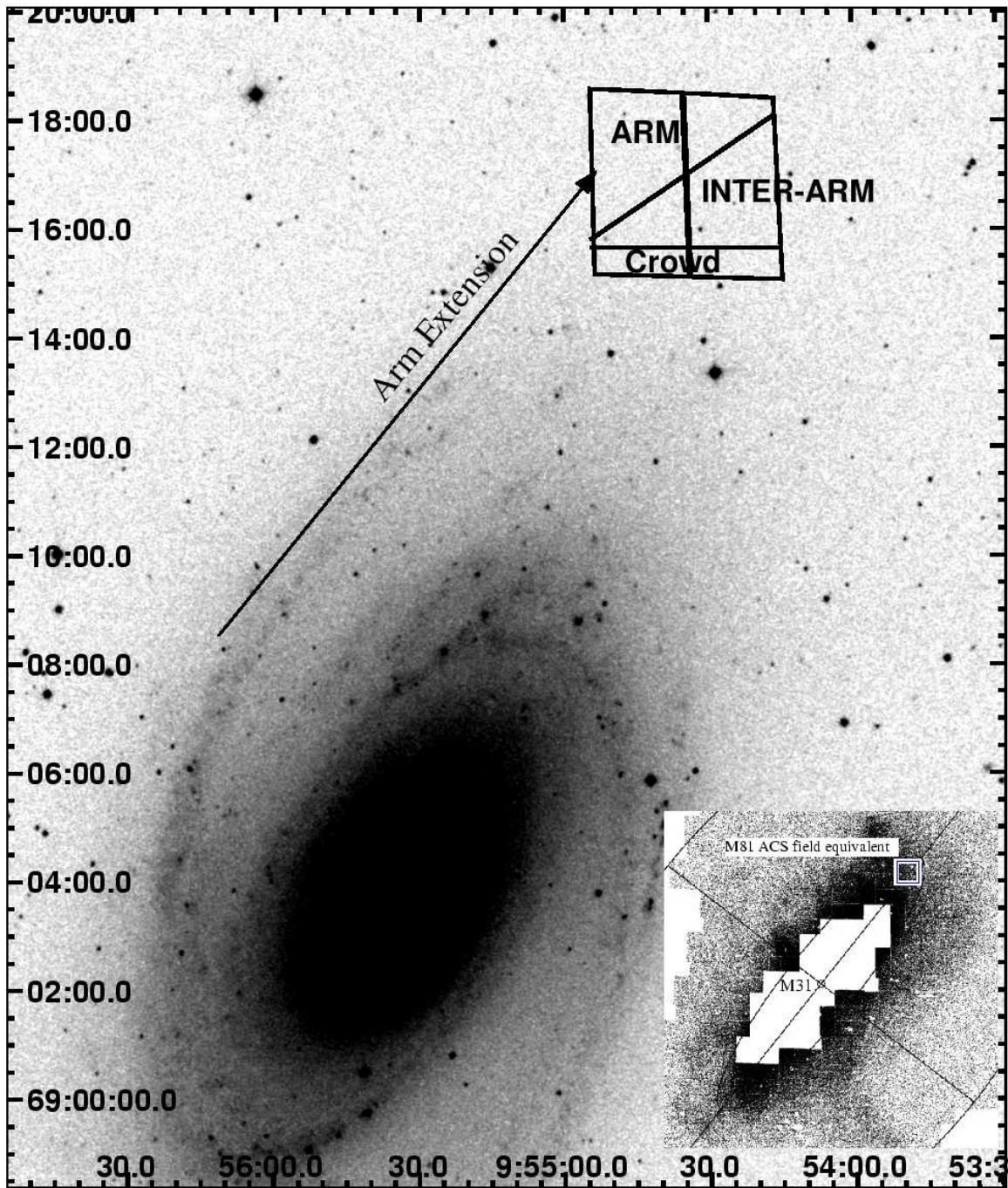


FIG. 1.— The locations of our M81-DEEP field and our defined subregions of the field shown on a DSS image. The arrow marks the apparent spur of the Northern spiral arm according to the distribution of main-sequence stars in our field. Inset on the lower-right corner is the equivalent location of our M81-DEEP field shown with a white box on a star count map of M31 (Ferguson et al. 2002). The inner and outer edges of the field are located at the same scale lengths as in M81.

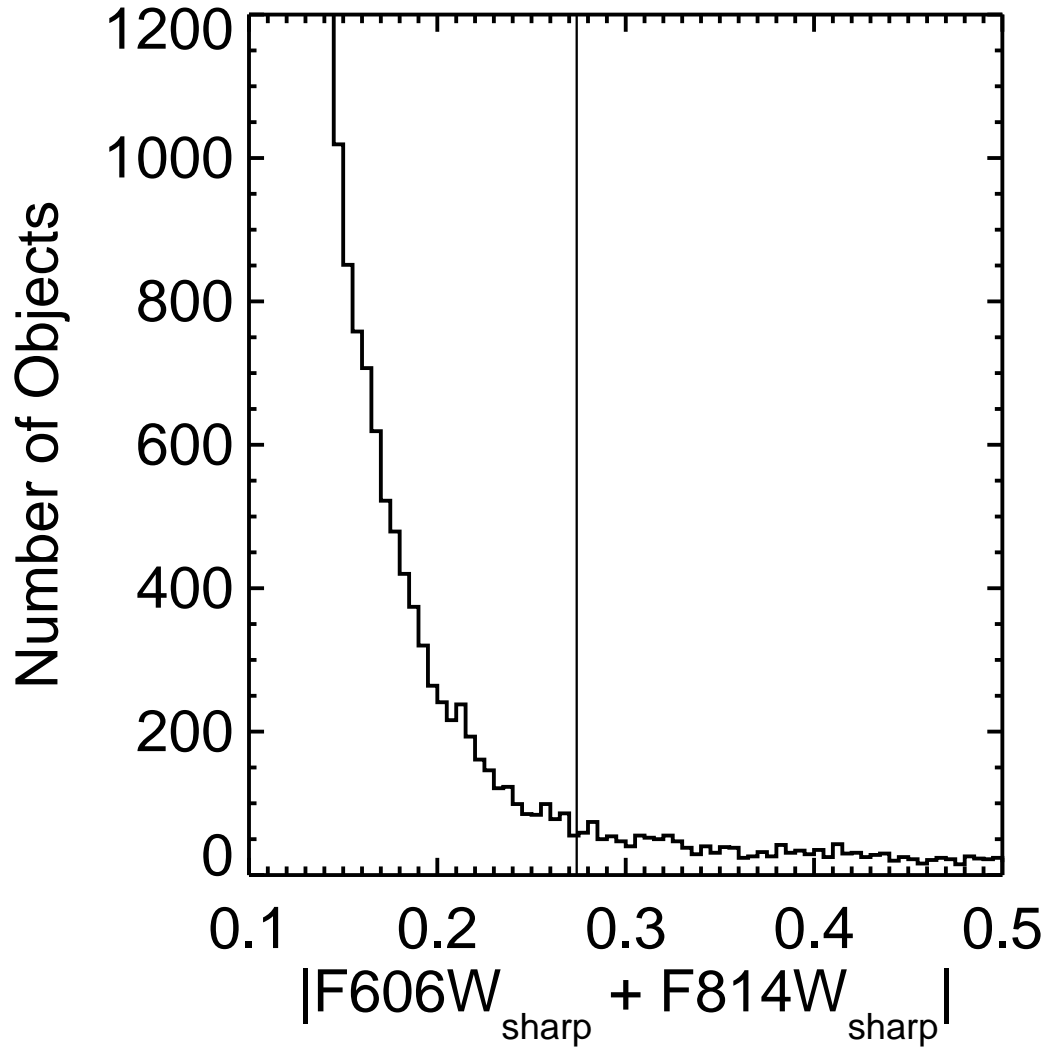


FIG. 2.— *Histogram*: The distribution of the combined sharpness values for objects in our initial photometry catalog. *Vertical Line*: The sharpness cut we applied to our final photometry catalog.

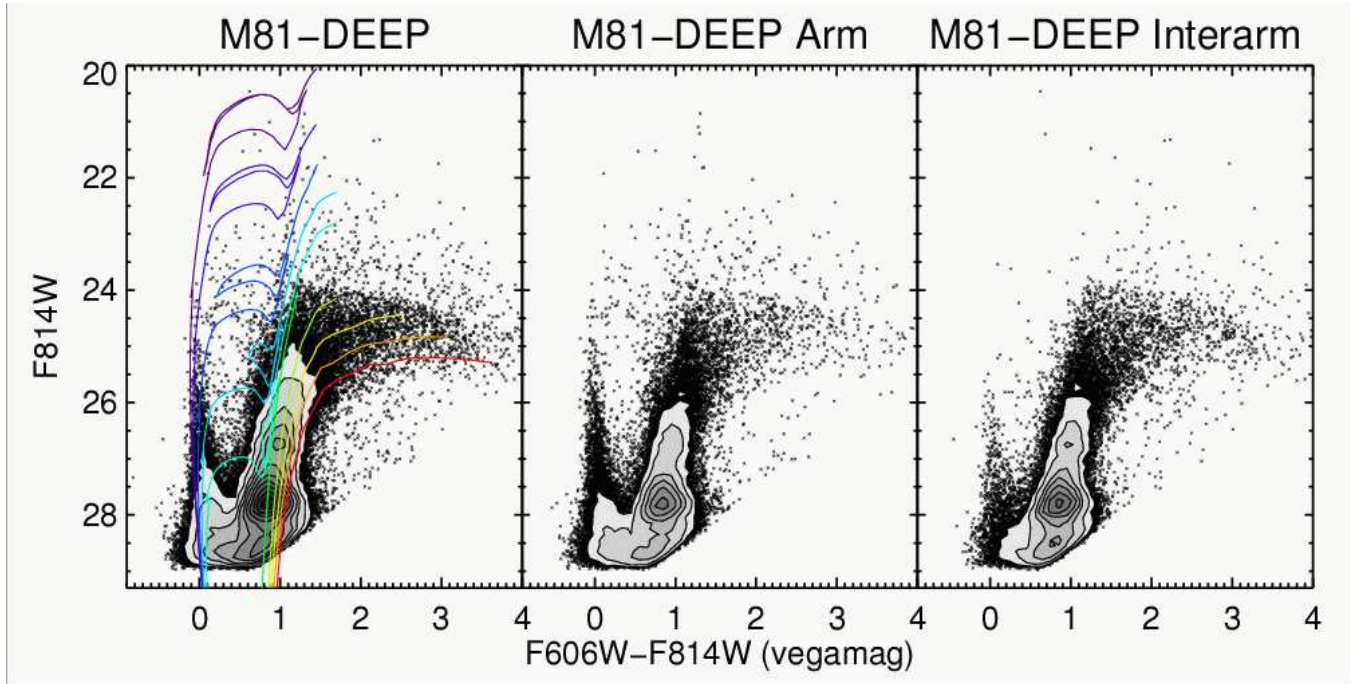


FIG. 3.— *Left:* The F606W, F814W CMD for our entire ACS field. Lines show a small subset of the isochrones used to fit the data (Marigo et al. 2008, shifted assuming $A_V = 0.3$ and $(m - M)_0 = 27.9$). Isochrones shown are (from blue to red): $[M/H]=-0.4$, $\log(\text{age})=7.3$; $[M/H]=-0.4$, $\log(\text{age})=7.6$; $[M/H]=-0.4$, $\log(\text{age})=8.0$; $[M/H]=-0.4$, $\log(\text{age})=8.3$; $[M/H]=-0.4$, $\log(\text{age})=8.6$; $[M/H]=-1.3$, $\log(\text{age})=10$; $[M/H]=-0.7$, $\log(\text{age})=10$; $[M/H]=-0.4$, $\log(\text{age})=10$; $[M/H]=-0.2$, $\log(\text{age})=10$; $[M/H]=0$, $\log(\text{age})=10$. *Middle:* The CMD of the arm region shown in Figure 4. *Right:* The CMD of the interarm region shown in Figure 4. In areas where the points would saturate the plot, we provide contours following the density of points in that part of the CMD.

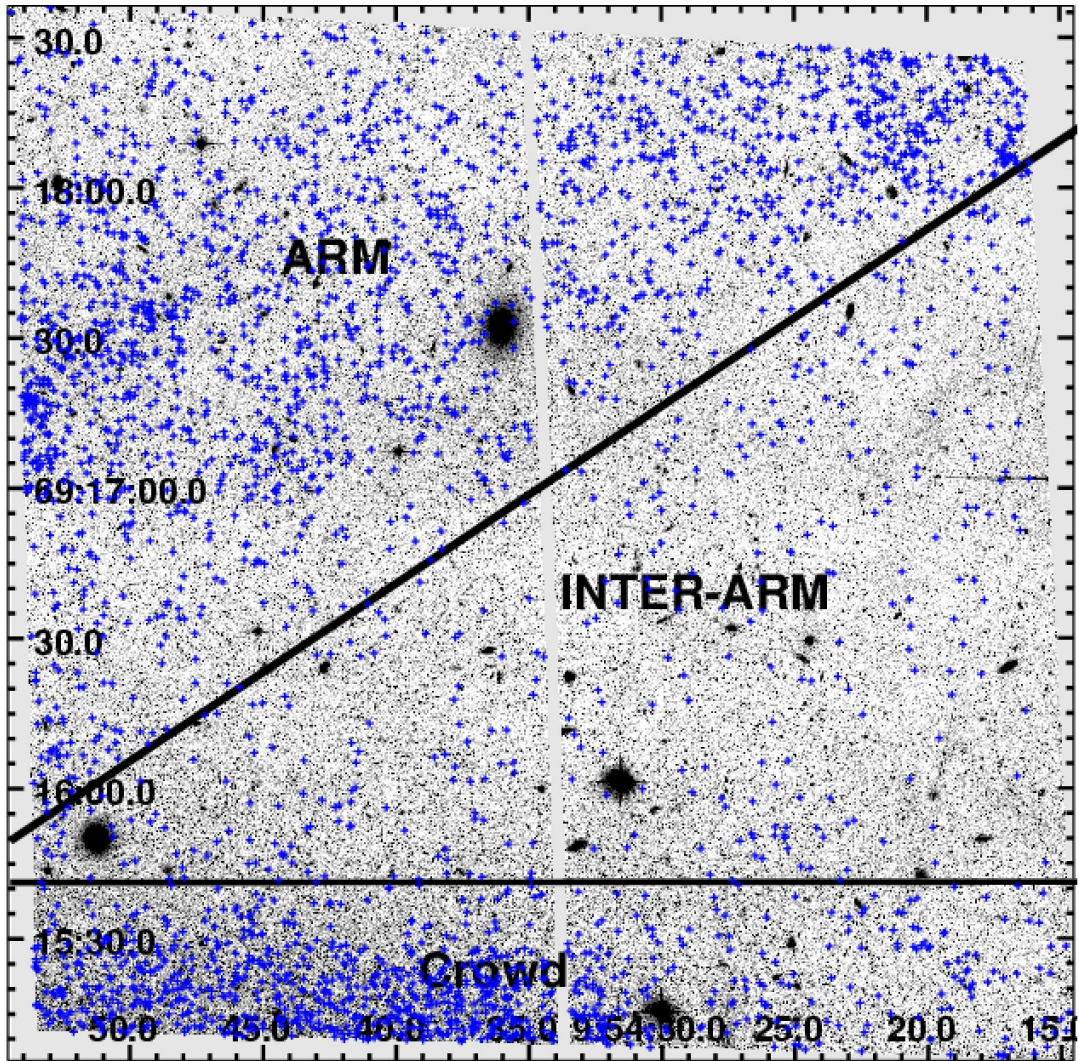


FIG. 4.— The borders of the subregions used in our SFH analysis. Blue crosses mark the locations of main sequence stars in the field. Main sequence stars were chosen using a hand-drawn polygon that followed the edges of the blue plume of stars in the CMD. The color and magnitude limits of the polygon were approximately $24 < F814W < 28$ and $-0.2 < F606W - F814W < 0.3$.

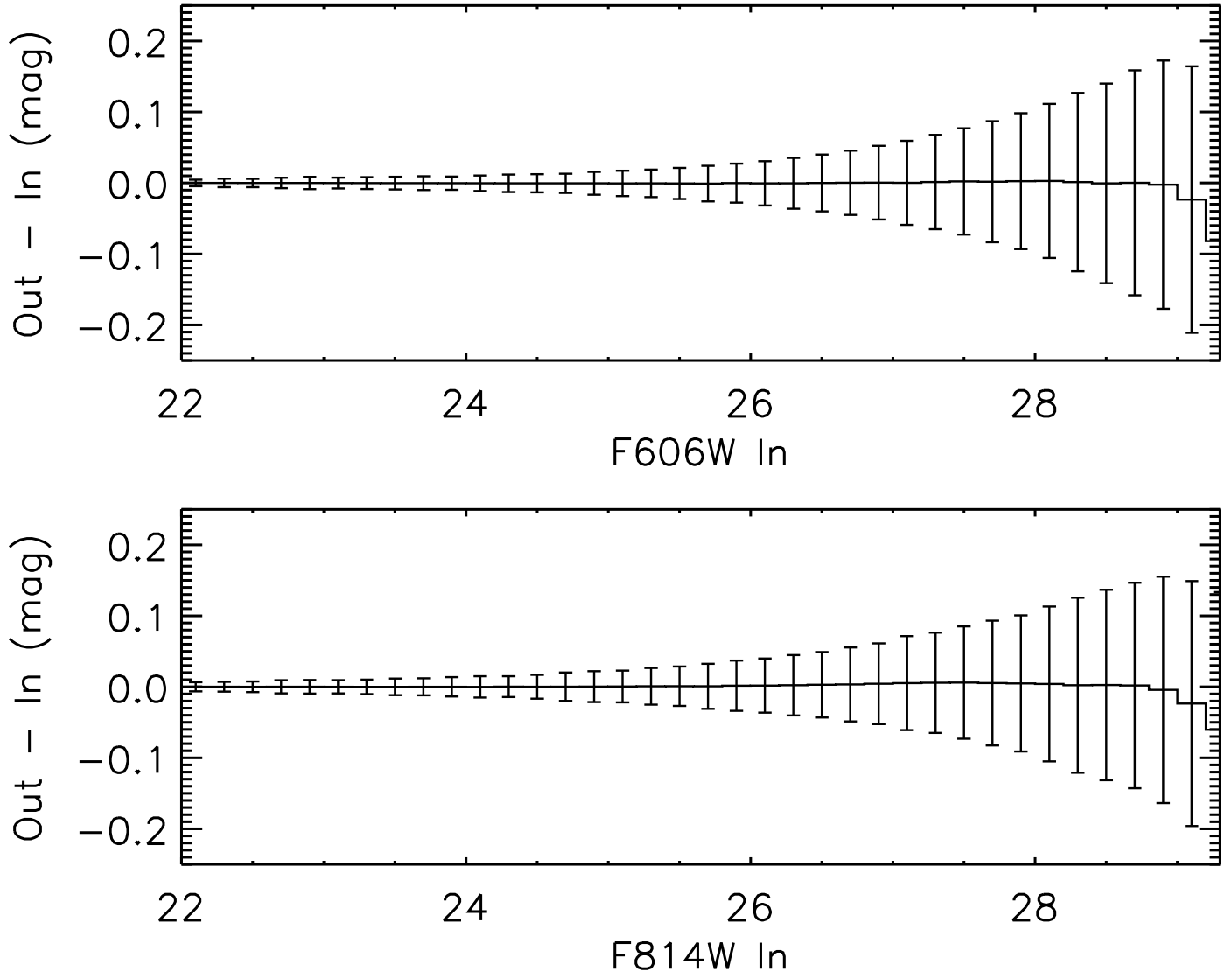


FIG. 5.— *Top*: The mean residual magnitude and root-mean-square error of the artificial star tests in the F606W filter measurements are shown as a function of input star magnitude. *Bottom*: Same as *Top*, but for the F814W filter measurements.

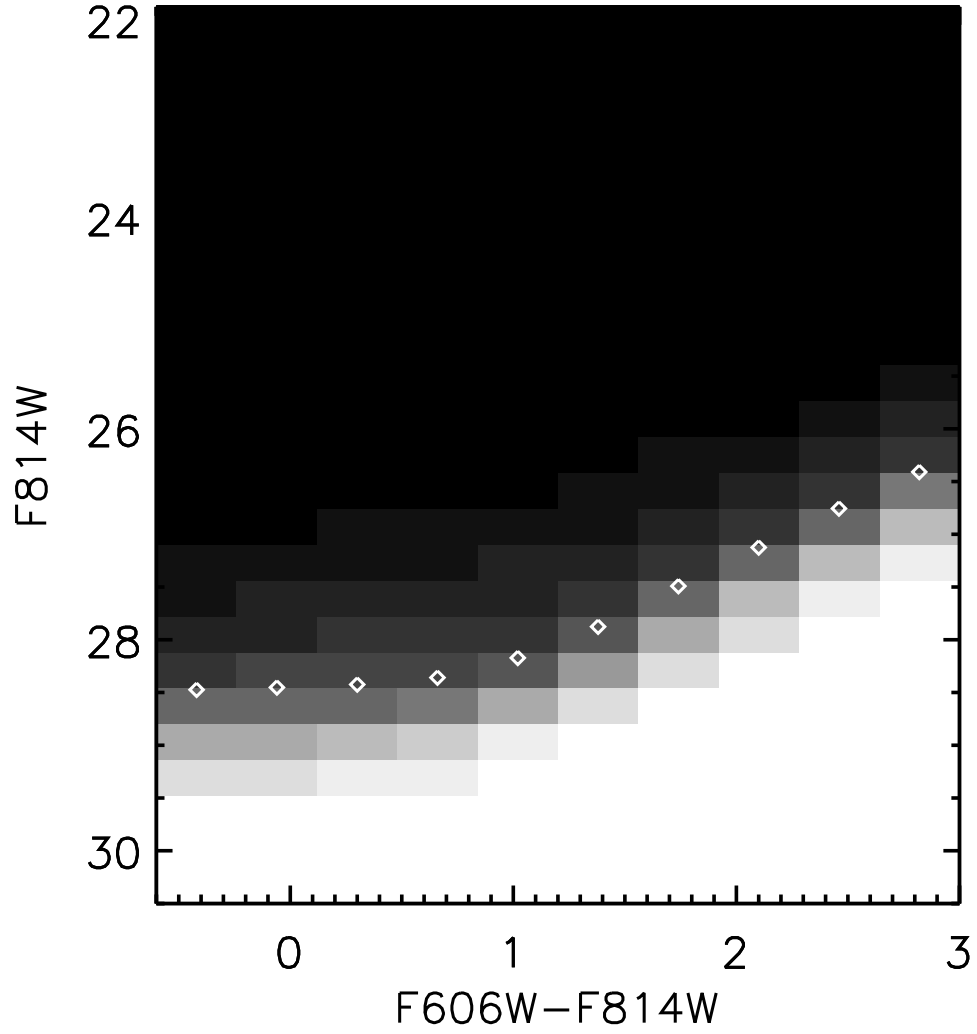


FIG. 6.— The completeness measured from our artificial star tests is shown in grayscale as a function of color and magnitude. The scale is linear, with 100% completeness shown as black and 0% completeness shown as white. White diamonds mark the completeness limit used to fit the SFH of the field.

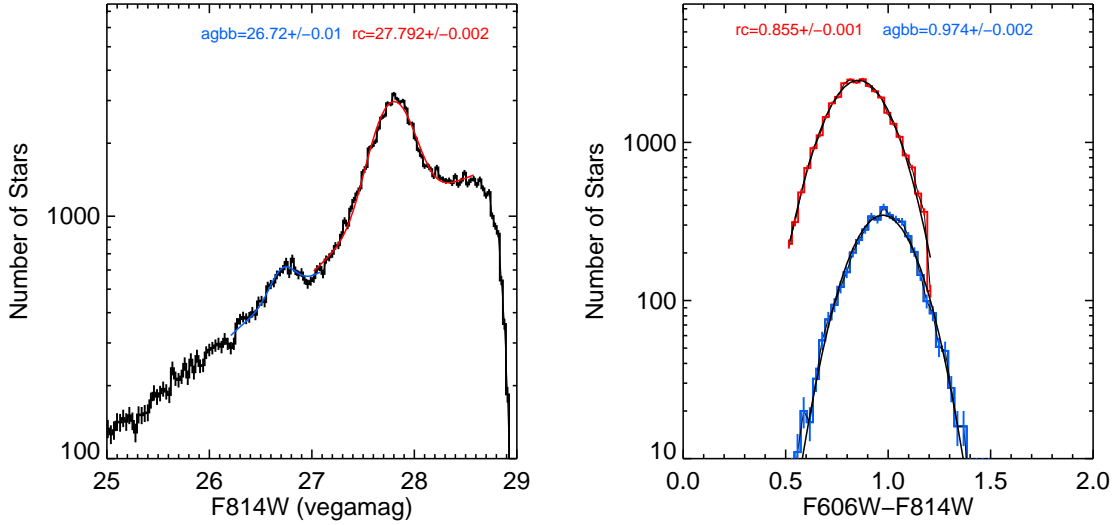


FIG. 7.— *Left*: Gaussian plus line fits to our measured magnitude histogram to determine the magnitude of the red clump (drawn in red) and AGB bump (drawn in blue). *Right*: Gaussian fits to the color histograms measured at the best-fit magnitude of the red clump (red) and AGB bump (blue).

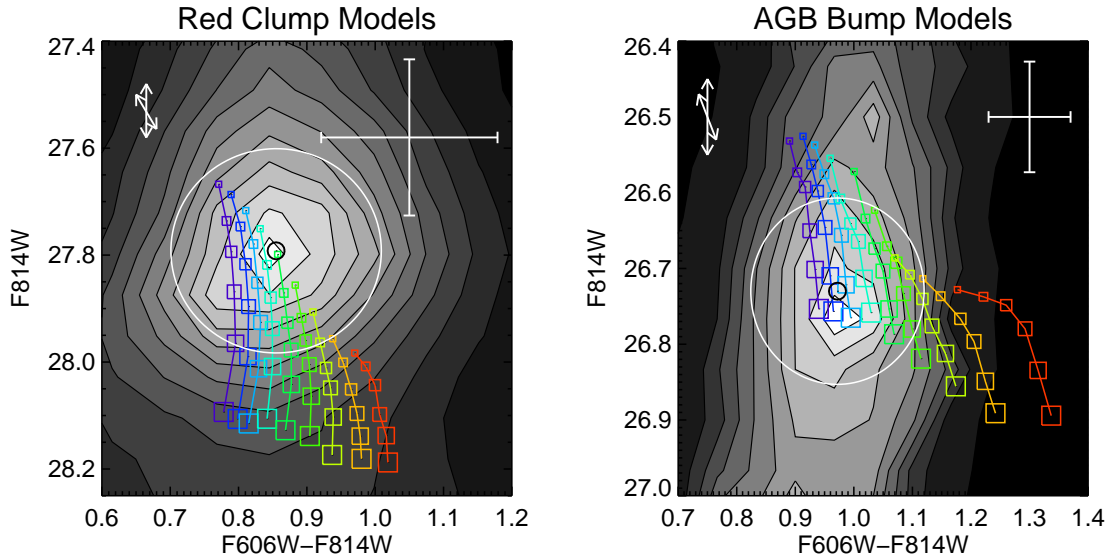


FIG. 8.— *Left*: Small portion of our full-field CMD centered on the red clump region. The black circle marks the best-fitting center for the feature. The white circle marks the measured height and width of the feature ($\sigma_{(m_{F606W}-m_{F814W})} = 0.154$; $\sigma_{m_{F814W}} = 0.191$). Boxes mark the locations of the fits to the same feature in model CMDs convolved with our photometric errors and completeness. Redder colors denote higher metallicities (the metallicity range is $-1.0 < [M/H] < 0.2$); larger boxes denote older ages ($2 \text{ Gyr} < \text{age} < 13 \text{ Gyr}$). Large error bars in the upper right show the 1-sigma width of the feature in a single age and metallicity CMD ($\sigma_{(m_{F606W}-m_{F814W})} = 0.129$; $\sigma_{m_{F814W}} = 0.146$). Arrows show our 1-sigma error ranges for distance and reddening. (*Right*: Same as *Left*, but for a small portion of our full-field CMD centered on the AGB bump region. The measured height and width of the feature are $\sigma_{(m_{F606W}-m_{F814W})} = 0.148$ and $\sigma_{m_{F814W}} = 0.123$. Values for the 1-sigma width of the feature in the a single age and metallicity CMD are $\sigma_{(m_{F606W}-m_{F814W})} = 0.070$ and $\sigma_{m_{F814W}} = 0.073$). Note the fitted AGB bump center is slightly brighter than the mode value due to the slope of the luminosity function skewing the mode to fainter magnitudes. Predicted magnitudes assume $A_V = 0.3$ and $(m - M)_0 = 28.0$.

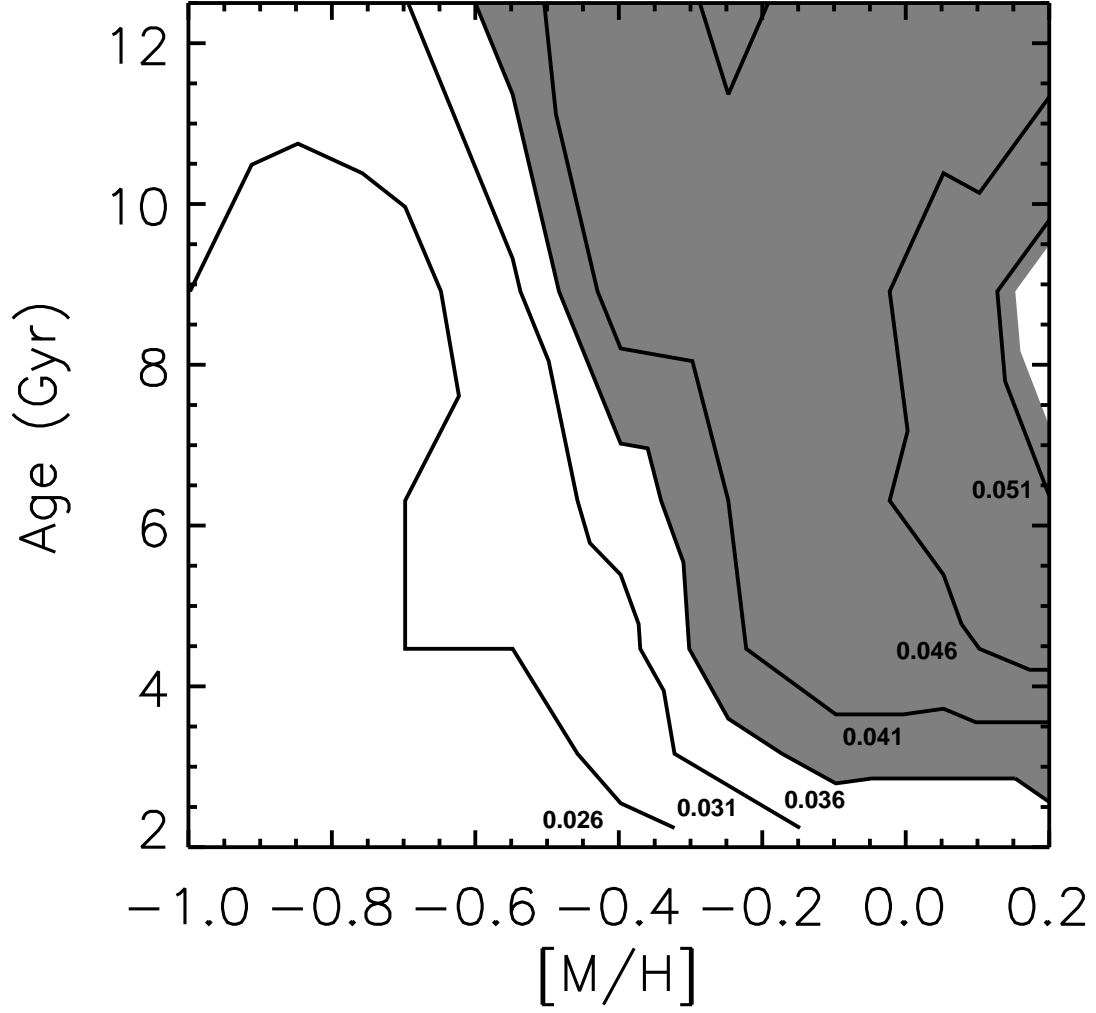


FIG. 9.— The age-metallicity plane. Contours denote different $N_{AGBb} : N_{RC}$ ratios, increasing from 0.026 to 0.051 from left to right and labeled. The shaded area denotes where model stellar populations have a ratio $N_{AGBb} : N_{RC}$ consistent with that measured from our data.

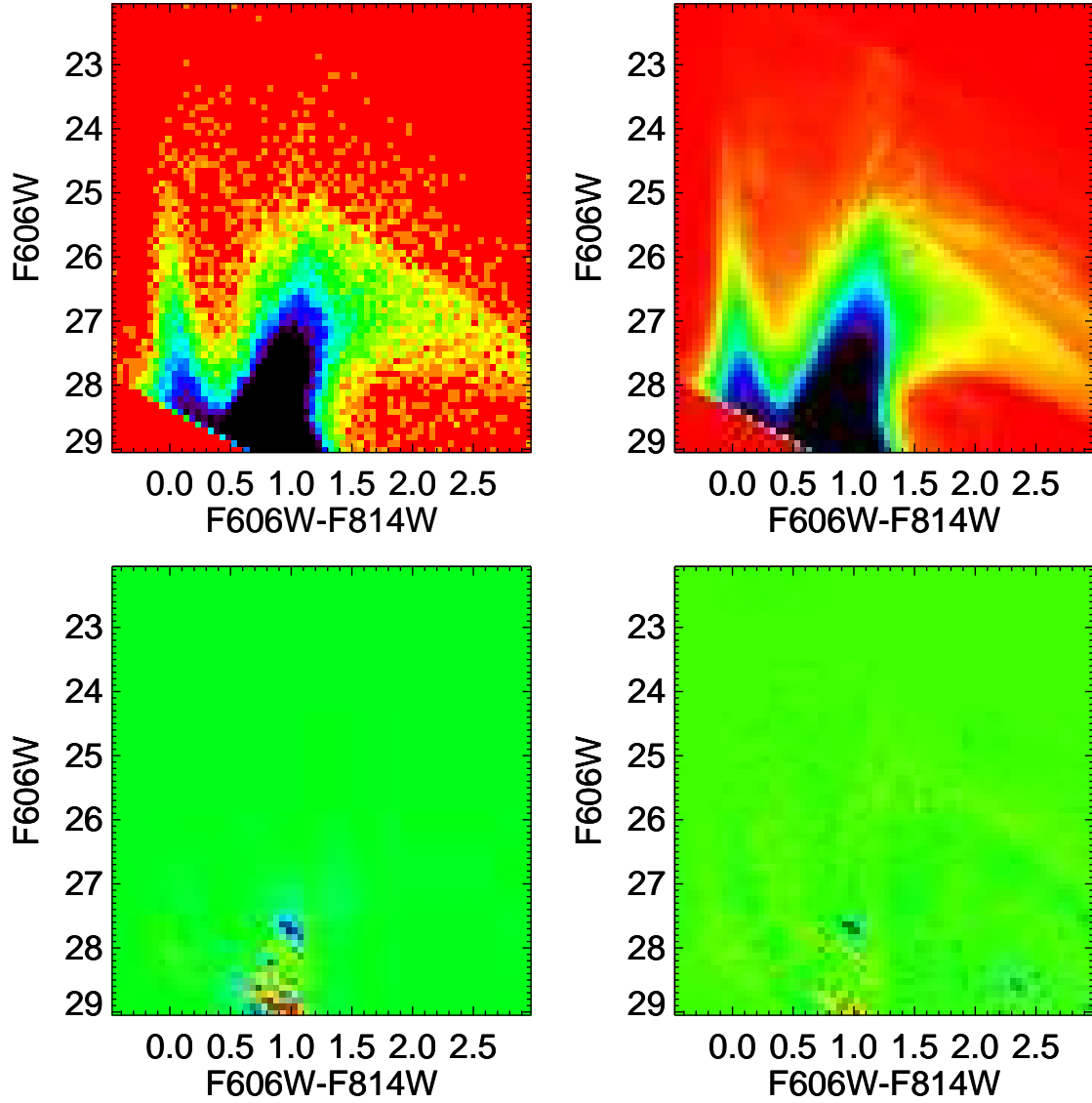


FIG. 10.— Our best full CMD fit to the data from the entire field. *Upper-left:* The observed CMD. *Upper-right:* The best-fitting model CMD from MATCH. *Lower-left:* The residual CMD. Redder colors denote an overproduction of model stars. Bluer colors denote an underproduction of model stars. *Lower-right:* The deviations shown in *lower-left* normalized by the Poisson error in each CMD bin. This plot shows the significance of the residuals in *lower-left*. Only the red clump and AGB bump show significant residuals.

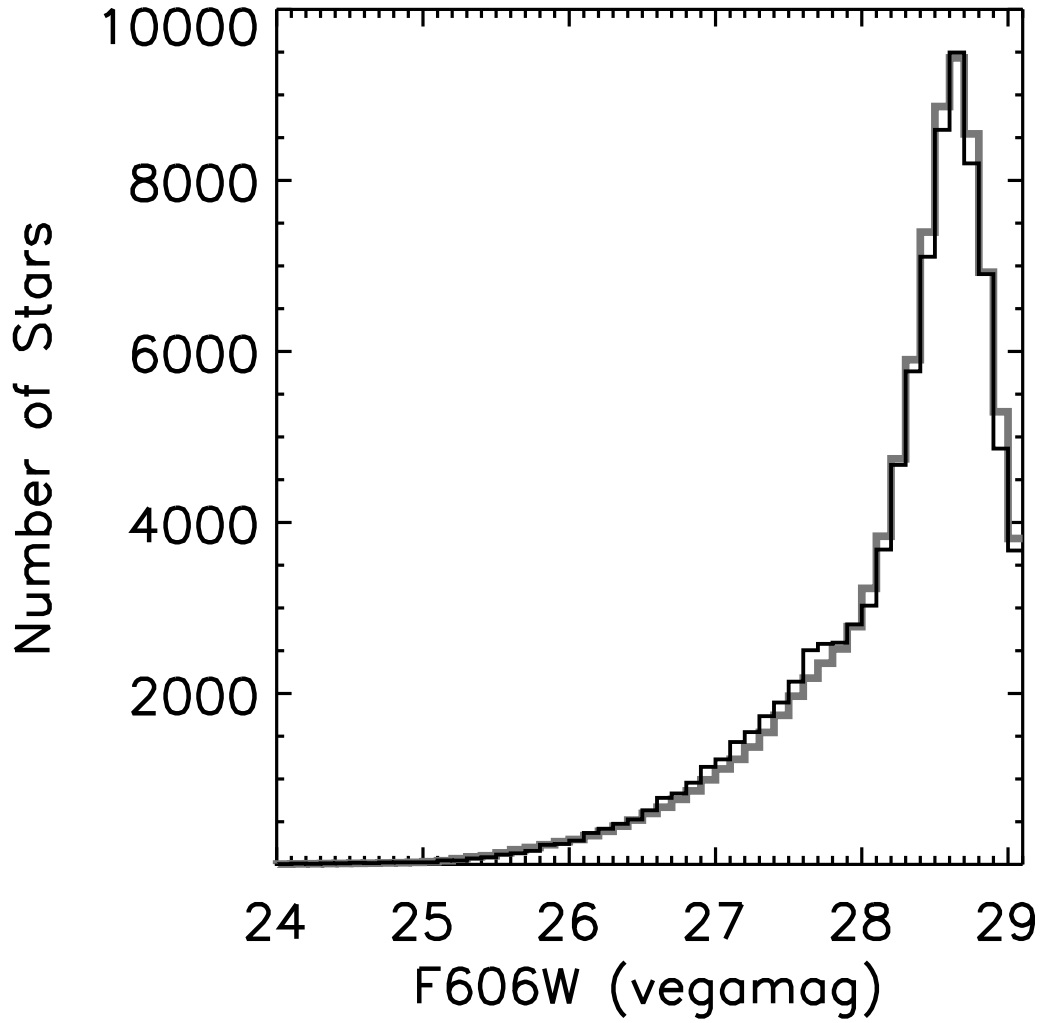


FIG. 11.— Histograms of the luminosity functions of our best full CMD fit to the data from the entire field. *Black*: The observed luminosity function of the entire field. *Gray*: The luminosity function of the best-fit model CMD.

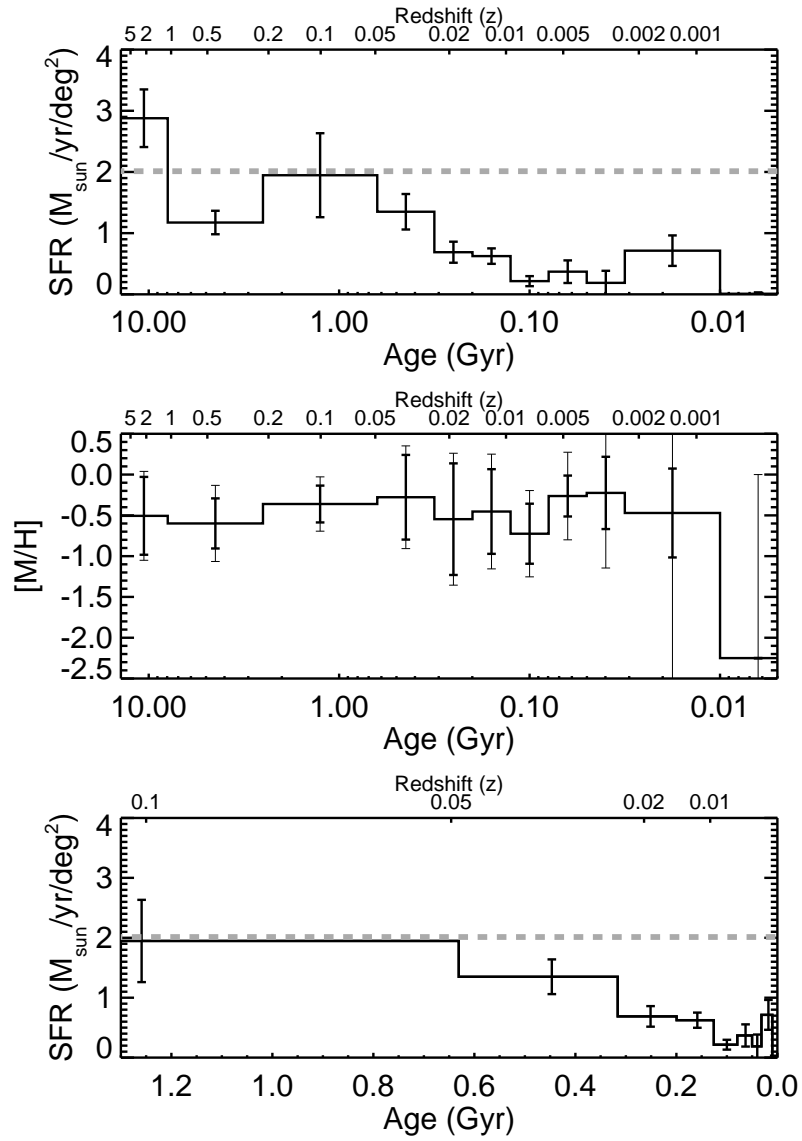


FIG. 12.— The SFH of the entire ACS field as determined by the MATCH package. *Top*: The solid histogram marks the star formation rate (normalized by sky area) as a function of time for the past 14 Gyr. The dashed line marks the best-fitting constant star formation rate model. *Middle*: The mean metallicity and metallicity range of the population as a function of time. Heavy error bars mark the measured metallicity range, and lighter error bars mark how that range can slide because of errors in the mean metallicity. *Bottom*: Same as *top*, but showing only the results for the past 1.3 Gyr.

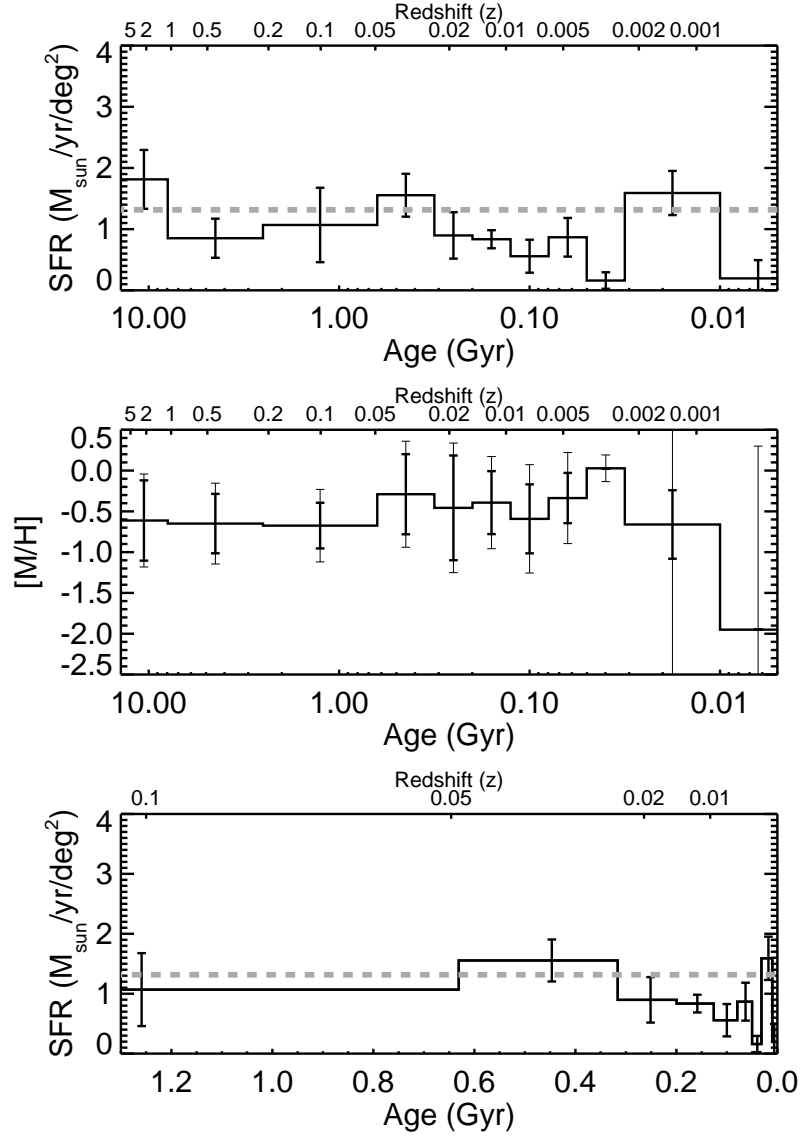


FIG. 13.— The SFH of the arm subregion as determined by the MATCH package. Lines, error bars, and panels are the same as in Figure 12.

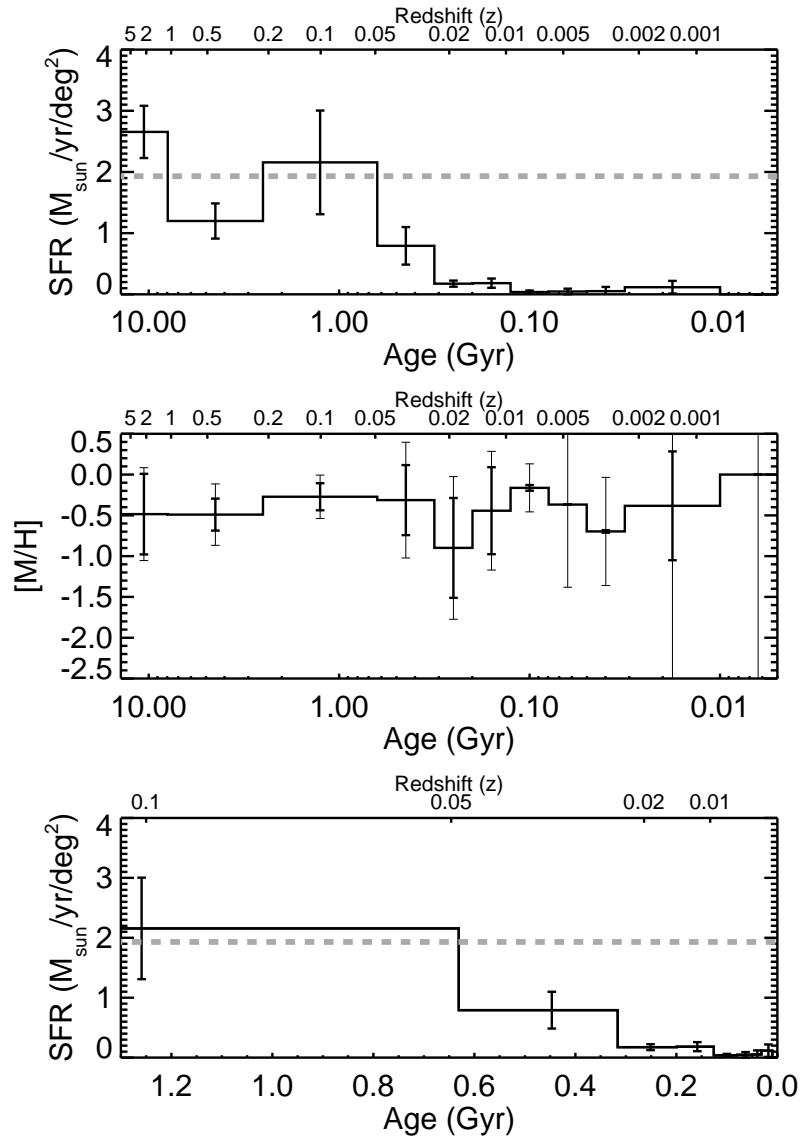


FIG. 14.— The SFH of the interarm subregion as determined by the MATCH package. Lines, error bars, and panels are the same as in Figure 12.

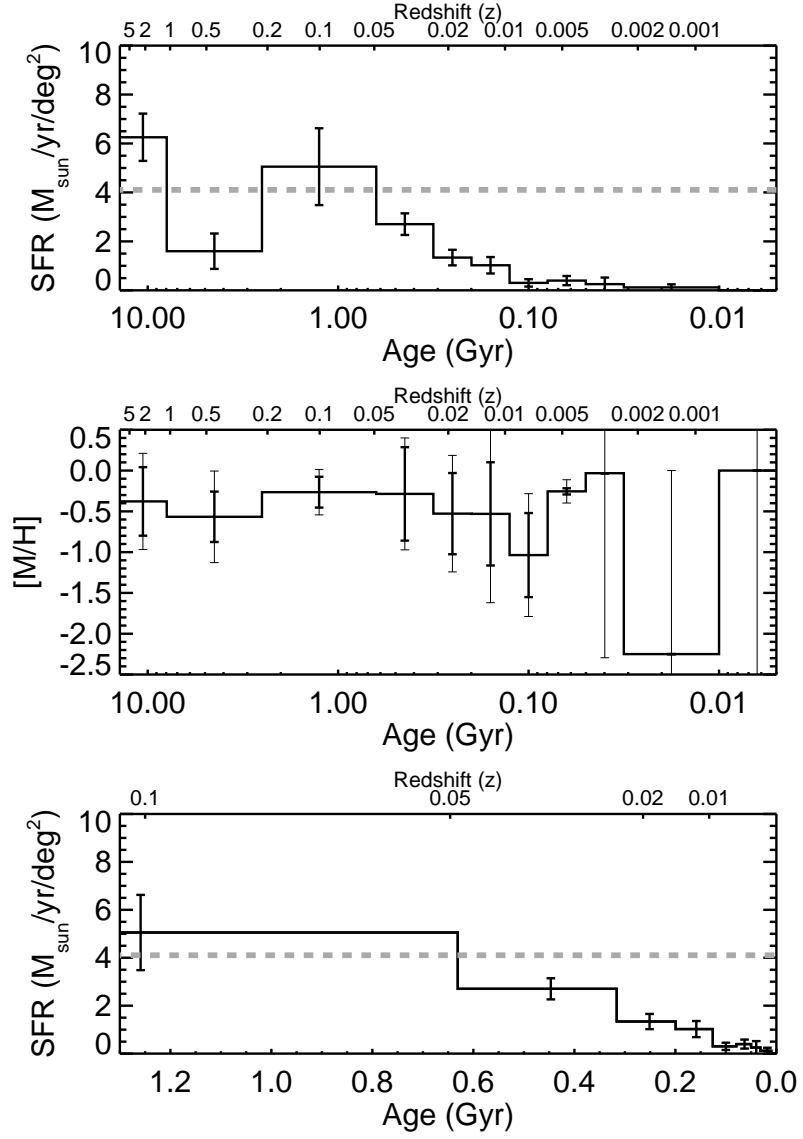


FIG. 15.— The SFH of the crowded southern subregion as determined by the MATCH package. Lines, error bars, and panels are the same as in Figure 12.

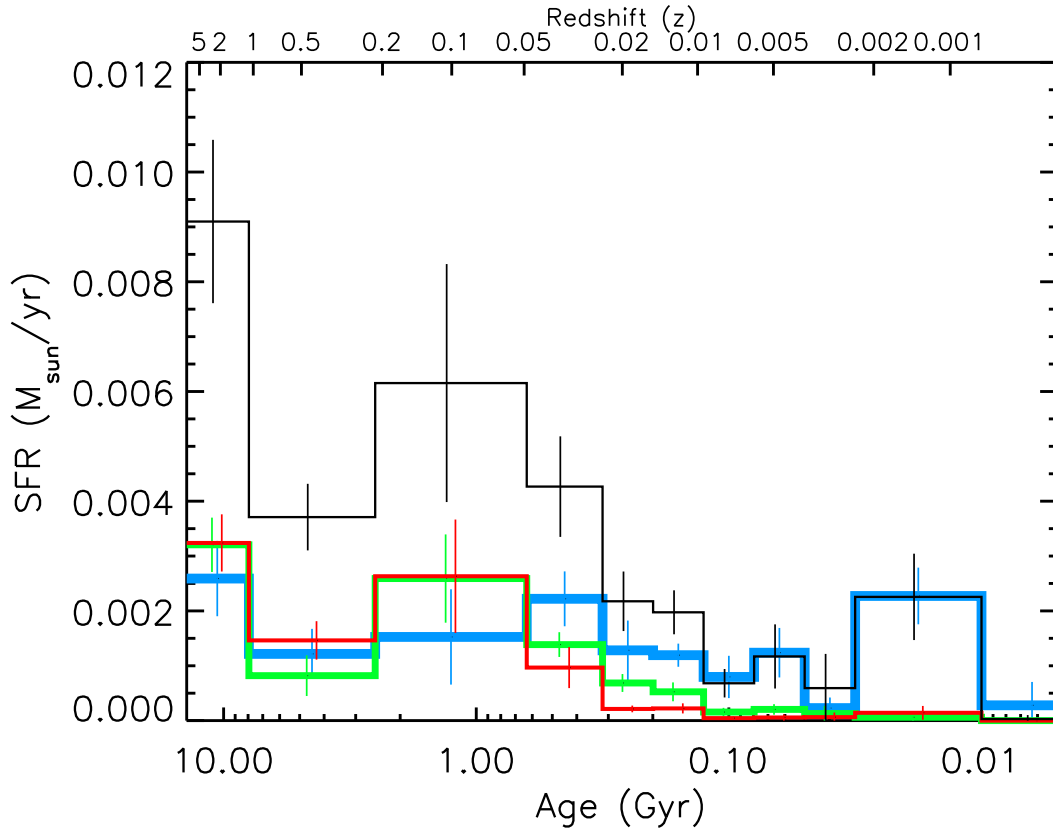


FIG. 16.— The SFH of all subregions are overplotted. Rates are not normalized by area in order to show the contribution of each subregion to the star formation of the total field. *Black*: The SFH of the full field as determined by the MATCH package. *Blue*: The SFH of the arm subregion as determined by the MATCH package. *Green*: The SFH of the crowded, southern subregion as determined by the MATCH package. *Red*: The SFH of the interarm subregion as determined by the MATCH package.

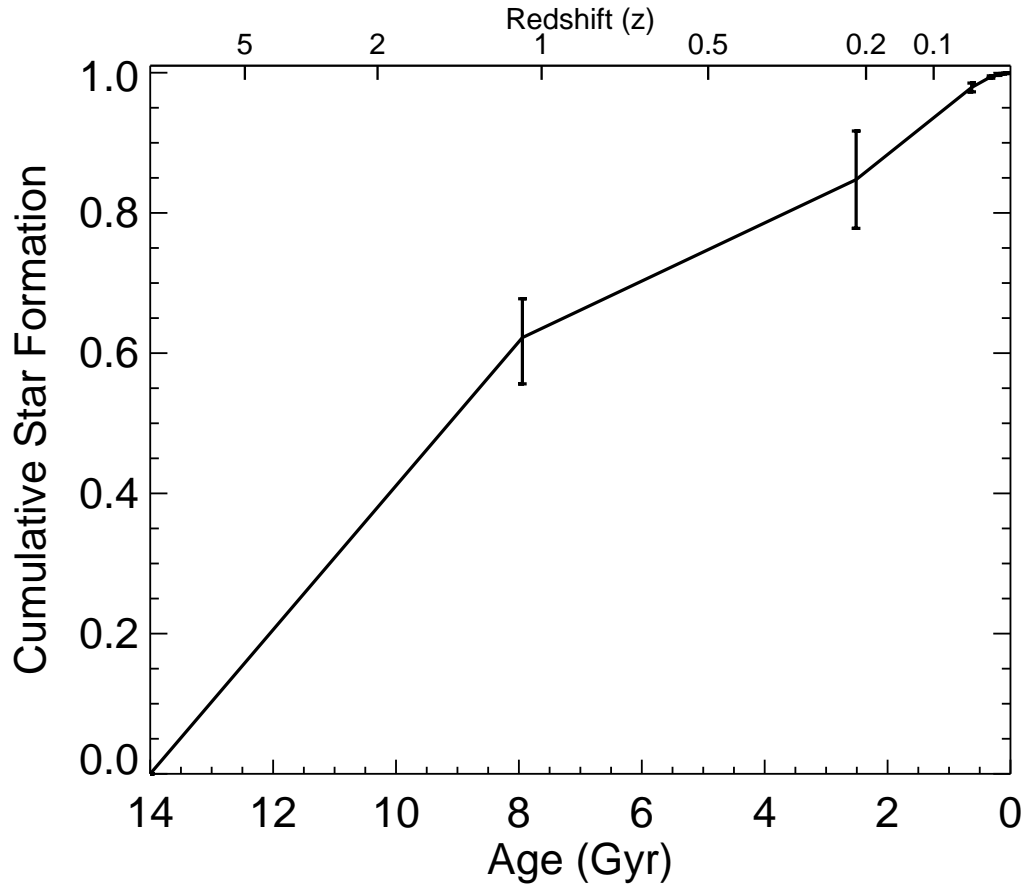


FIG. 17.— *Black*: The normalized cumulative star formation of the full field as determined by the MATCH package.

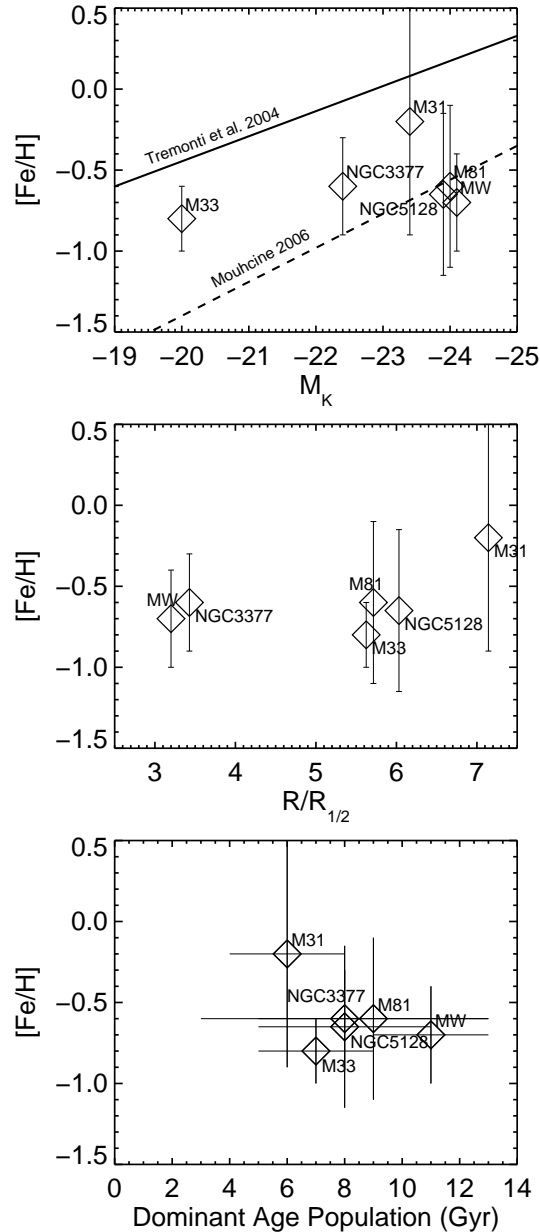


FIG. 18.— Metallicity range of the dominant stellar populations in deep resolved photometry for M31 (Brown et al. 2006), M33 (Barker et al. 2007), M81 (this work), NGC 5128 (Rejkuba et al. 2005), and NGC 3377 (Harris et al. 2007) are plotted along with that of the Milky Way thick disk (Allende Prieto et al. 2006) against several other properties. *Top*: The metallicities as a function of the absolute K-band magnitude of the galaxy (Skrutskie et al. 2006). The solid and dashed lines show the luminosity-metallicity relations determined by Tremonti et al. (2004, gas phase metallicity of galaxy central regions) and Mouhcine (2006, stellar red peak metallicities of galaxy “halos”), respectively. These relations were converted from B-band and V-band to K-band using the Tully-Fisher calibrations of Verheijen (2001) and Sakai et al. (2000). The Milky Way luminosity was calculated by applying $V_{rot} = 220 \text{ km s}^{-1}$ to the Tully-Fisher calibration of Verheijen (2001). *Middle*: The populations’ metallicities as a function of the radii at which they were sampled (normalized to the half-light radius of the galaxy). *Bottom*: The populations’ metallicities as a function of their ages.